

MATERIAL SCIENCE & BATTERY RESEARCH

PRESENTING INKARP'S **LABSTATION i**
INERT GAS GLOVEBOX WORKSTATION



EXPLORE METALLIC GRAIN
STRUCTURES WITH
**ZEISS MICROSCOPY
SOLUTIONS**

SCANNING MICROWAVE MICROSCOPY (SMM) - A MODERN
ALTERNATIVE TO SCANNING CAPACITANCE
MICROSCOPY (SCM)



23-24-25 April 2025, Mumbai
Booth No: G031



39+ Years of Pioneering the Scientific Frontier

Inkarp, established in 1985, honors 39 years of dedication to the scientific community in India. Our journey continues to be driven by the pursuit of excellence in **offering cutting-edge scientific research instruments**. We take pride in providing scientists across the country with tools that facilitate discoveries and innovation.



Scan
to view our website

Follow Us On





From the editor

Dear Readers,

I am **thrilled** to present to you the 4th issue of CATALYSTCue, where we delve into the **fascinating** world of **Material Science and Battery Research**.

Our cover story takes you into the heart of a **pioneering** research lab where a dedicated team has made an **exciting breakthrough**—developing a **graphene coating** that makes glass **scratch-proof**. This **simple yet powerful** innovation not only enhances the **durability** of glass but also opens new doors for its use in **demanding environments**.

In this issue, we also dive deep into the **complex world of plastics manufacturing** and explore how cutting-edge **analytical techniques** are helping optimize process conditions. We also shed light on a **critical aspect of lithium-ion battery production**—how the presence of **water**, even in **trace amounts**, can severely impact battery **performance** and **longevity**. Understanding these nuances is crucial, especially as we move towards a future increasingly reliant on **sustainable energy solutions**.

The **application stories** in this issue are particularly **exciting**. You'll read about how **automation** is **revolutionizing high-throughput battery development**, explore the **microscopic world of metallic grain structures**, **evaluate recycled polymers**, and analyse the **chemical stability of lithium-ion battery electrolytes**—a key factor in enhancing battery **safety** and **efficiency**.

Graphene enthusiasts will find our exploration into **nanoscale analysis using atomic force microscopy**, particularly **engaging**. There's a deep dive into **advanced battery component analysis**, offering a **comprehensive view of how modern tools** are pushing the boundaries of what's possible. We also discuss techniques to detect **thermal degradation of polymers**, vital for improving product **safety** and **durability**.

Our Tech Corner introduces **Scanning Microwave Microscopy (SMM)**, an **innovative technique** offering a **fresh perspective on surface characterization**. We also outline a practical guide on **annealing** process using a **muffle furnace**.

We spotlight a **versatile inert gas glovebox workstation** in our Product Highlight—an **essential tool** for labs handling **sensitive materials**.

Science thrives on **curiosity** and the **relentless pursuit** of understanding, and it's my hope that CATALYSTCue continues to be a small part of that journey for you.

Your **feedback** means a lot to us, and I'd love to hear your thoughts.

Best regards,

Arun Mathrubootham
Director
Inkarp Instruments Pvt. Ltd.

FEBRUARY 2025

Volume 01 Issue 04

Contents

03

Cover Story

03 Graphene- The Scratch-Proof Solution

04

Features

04 Optimising process conditions and ensuring end product requirements of plastics with rheological analysis

12 Water- Poison for Lithium-ion Batteries

16

Interview

16 Interview- Significance of Glovebox in Battery Testing

Dr. Anil Suryawanshi,

Associate Technical Specialist, KPIT Technologies Ltd.

21

Application Showcase

21 Automatic Detection of the Thermal Degradation of a Polymer using the Thermo Scientific HAAKE MARS Rheometer.

- 24** Measuring Hydrofluoric Acid Content of Lithium-ion Battery Electrolyte in the Mettler Titration Excellence T5.
- 28** Evaluation of Recycled Polymers by Thermal Analysis using Hitachi High-Sensitivity Differential Scanning Calorimeter and Simultaneous Thermogravimetric Analyzer.
- 33** In Situ FT-IR Spectroelectrochemistry using a Bruker VERTEX 80 FT-IR Spectrometer.
- 38** Metallic Grain Structures and Their Microscopic Analysis with Zeiss Microscopy Solutions.
- 47** Fully automated high-throughput battery development using the Chemspeed FLEXSHUTTLE.
- 52** Battery components analyses using NenoVision's AFM-in-SEM LiteScope™
- 56** Nanosurf's AFM Solutions as an Analysis Tool for Graphene.

61

Tech Corner

61 Scanning Microwave Microscopy (SMM) - A Modern Alternative to Scanning Capacitance Microscopy (SCM)

64 Guide: Optimized Annealing of TiO₂ and Tin for Enhanced Crystallinity and Reduced Thermal Stress

67

Product Highlight

67 Inkarp's Labstation i Inert Gas Glovebox Workstation

70

Industry Buzz

70 Recent novel FDA approved drugs

71 A sneak-peak at our events

FEBRUARY 2025

Graphene:- The Scratch-Proof Solution

In our everyday life, glass plays a ubiquitous role. Yet, this seemingly robust material is vulnerable to scratches, abrasions and the effects of moisture, affecting its long-term durability. Researchers from IIT-Delhi have discovered a remarkable solution: a thin layer of graphene, which can enhance the glass's resistance to wear and tear, even under humid conditions.

A team of scientists from Indian Institute of Technology Delhi, led by Dr. Nitya Nand Gosvami, Associate Professor Department of Materials Science and Engineering, and Dr. N.M. Anoop Krishnan, Associate Professor, Department of Civil Engineering, investigated the protective properties of graphene on silica glass, a common type of glass used in numerous delicate moisture-prone applications, such as in aerospace, telecommunications, optics etc.

Graphene, a 2D allotrope of carbon shows excellent frictional, mechanical and thermal behaviour, to name a few. Using this to their advantage, the research group demonstrated that the tribochemical wear resistance of silica significantly improved with few-layer graphene deposition.

Nano scratch experiments using the Nanosurf Drive AFM were conducted. This contact-mode atomic force microscopy was conducted using both chemically inert and reactive tips. Bare glass, as expected, exhibited significant wear and material loss under even moderate stress. The presence of water further exacerbated the damage, as water molecules penetrated the glass surface and weakened its structure. On the other hand, graphene coated glass showed $\approx 98\%$ reduction in friction with no material loss or visible damage.

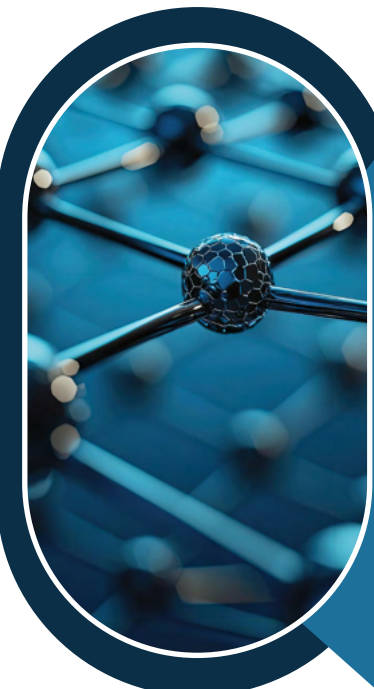
Compared to bare glass, graphene-coated glass exhibited $\approx 98\%$ reduced friction

This research has significant implications for a wider range of applications including smartphone screens, aerospace components, optical devices etc. Both consumers and industries may benefit from less waste and lower costs as a result. The enormous potential of two-dimensional materials for developing advanced protective coatings have been explored in this study.

By combining high strength, chemical inertness and lubricity, graphene offers a powerful solution to the long-standing challenge of wear in glass.

Reference

Sahoo, S.; Khan, Z.; Mannan, S.; Krishnan, A.; Nitya Nand Gosvami. Graphene Mitigates Nanoscale Tribochemical Wear of Silica Glass in Water. *Small* 2024. <https://doi.org/10.1002/smll.202410040>.



Optimizing process conditions and ensuring end product requirements of plastics with rheological analysis

ThermoFisher
SCIENTIFIC

Authors

Fabian Meyer, Senior Rheology Application Specialist

Nate Crawford, Rheology Application Specialist

Keywords

Polymers, melt, viscoelasticity, molecular weight, processing, DMTA, extensional testing

Introduction

Plastics are polymeric materials that are used in a wide range of applications and for a broad variety of consumer products. In order to make these products, polymers are commonly processed at elevated temperatures in a molten state. Understanding how these melts deform, and flow is key to knowing how to effectively process and transform them into the end products we readily consume.

Due to their chemical structure and high molecular weight, polymer melts exhibit a complex flow and deformation behaviour. They are considered viscoelastic materials, showing both viscous (liquid-like) and elastic (solid-like) properties. A good knowledge of the viscoelastic

properties of a polymeric material is essential to optimize formulations and blends as well as to adapt a process to the properties of a given material. The molecular structure as well as the testing or processing conditions of a polymer melt determine which behaviour is dominant (viscous or elastic). Too much elasticity can lead to flow anomalies and unwanted effects during many common processing steps¹. One example is the swelling of a melt stream exiting the narrow die of an extruder. Other examples of flow anomalies caused by elastic properties of polymeric fluids are shown in Figure 1.

Capillary viscometers and melt flow indexers are frequently used to measure the melt viscosity of polymers. However, these instruments will not provide any information about the viscoelastic properties of the tested sample. Rotational rheometers with the capability to perform rheological tests with small oscillatory mechanical excitations on the other hand, allow for a comprehensive investigation of these properties.

This report is intended to give an overview of the different rheological tests that can be performed with rotational rheometers and explain how the obtained results relate to different processing conditions as well as to the final product properties.



Die swell

Sharkskin

Melt fracture

Rod climbing

Figure 1: Typical flow anomalies of viscoelastic polymer fluids.

Rotational vs. oscillatory testing

The Cox-Merz rule

Rheology has proven to be an excellent tool to analyse the mechanical properties of polymers in their different physical states. Various testing methods can be utilized to fully characterize the rheological behaviour of polymeric materials. Though rotational steady state shear experiments allow for measuring the non-Newtonian viscosity of dilute and semi-dilute polymer solutions, the preferred testing methods for polymer melts (and solids) utilize the application of an oscillatory shear deformation. This is due to their high elasticity and the consequential occurrence of edge failures when exposed to large deformations in a rotational rheometer. According to the Cox-Merz rule, the complex viscosity ($I\eta^*I$) derived from oscillatory frequency sweep measurements plotted against the angular frequency (ω) is identical to the steady state shear viscosity from rotational testing plotted against the shear rate². The Cox-Merz rule is an empirical rule that is valid for many polymer melts and polymer solutions. Figure 2 shows the comparison of viscosity data obtained from rheological tests in rotation and in oscillation mode.

Once the end of the Newtonian (zero shear viscosity) plateau is reached and the viscosity starts to decrease, the shear viscosity (red symbols) drops abruptly and no longer displays a continuous, smooth progression. The observed drop is due to sample fracture at the edge of the measuring geometry caused by secondary flow fields¹. The oscillation frequency sweep (green symbols), on the other hand, provides higher data quality across a broader frequency range.

The improved testing range of the oscillatory frequency sweep is due to the small amplitudes of the imposed oscillatory shear. As a result, performing an oscillatory frequency sweep and applying the Cox-Merz rule is the preferred method for obtaining shear viscosity data for polymeric materials.

Identifying the linear-viscoelastic range

The amplitude sweep tests

In order to obtain comparable viscosity data from a frequency sweep experiment (as discussed above), the applied sinusoidal oscillatory deformation must be relatively small and within a material's linear viscoelastic range (LVR). In this range, the material's microstructure remains unchanged and as a result, the rheological properties such as the storage and the loss modulus (G' and G'' , respectively) or the complex viscosity are constant and independent of the applied stress or deformation. Once a critical deformation or stress value is reached, the microstructure of the material begins to change, and the rheological parameters start to change.

The linear viscoelastic range of a material is determined by performing an oscillation amplitude sweep test. During this test, which is performed at a constant frequency, the sinusoidal deformation or stress applied by the rheometer is gradually increased. Figure 2 shows the results of an amplitude sweep for LDPE at 190 °C. The end of the linear viscoelastic range of this LDPE melt was calculated automatically by the rheometer software and is equal to a deformation of 55 %.

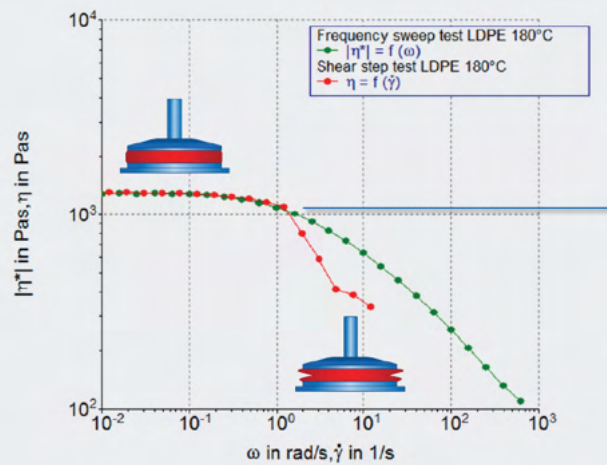


Figure 2: Comparison of viscosity data obtained from a steady state shear (red symbols) and an oscillation frequency sweep test (green symbols).

Further tests in oscillation mode, such as frequency, temperature, or time sweep tests, should be performed at a deformation below this critical value (unless the test is intended to be outside the LVR). When a frequency sweep test is performed over a wider frequency range (several orders of magnitude), it is recommended to perform several amplitude sweeps at different frequencies, in order to make sure that the selected deformation remains within the LVR across the entire frequency range.

Viscoelastic fingerprint of a material

The frequency sweep test

The information gained from the rheological tests in oscillation mode is manifold. For instance, shear rate dependent viscosity data derived from oscillatory frequency sweep experiments, together with the

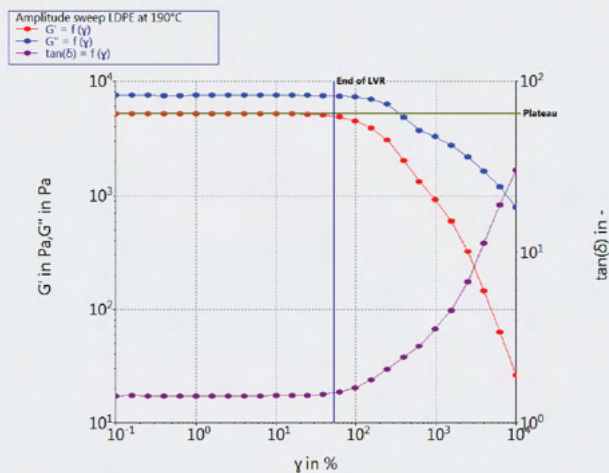


Figure 3: Storage modulus G' , loss modulus G'' and the complex viscosity G^* as a function of the deformation γ for a LDPE melt at 1 Hz and 190°C.

utilization of the Cox-Merz rule, allow for quantifying the flow resistance of a material during high shear processing applications such as extrusion or injection moulding.

The low frequency/shear data (zero shear viscosity, η_0), on the other hand, can be used to calculate the weight average molecular weight (M_w) of a polymer melt according to:

$$\eta_0 = k \cdot M_w^{3.4} \quad (1)$$

The prefactor k depends on the molecular structure of the polymer³. Equation 1 is valid for polymers with a linear chain structure and a molecular weight above a critical value (M_c). Figure 4 shows a typical viscosity curve of a polystyrene melt and the corresponding shear rate ranges that occur in common processing applications.

Besides information about the overall flow resistance, frequency sweep data also provides a direct measure of the viscous and elastic properties of a polymer. These are represented by the storage and the loss moduli (G' and G'' , respectively) measured at different frequencies/time scales.

The data reveals the general structure of a material and also provides information of the molecular weight (M_w) and the molecular weight distribution (MWD).

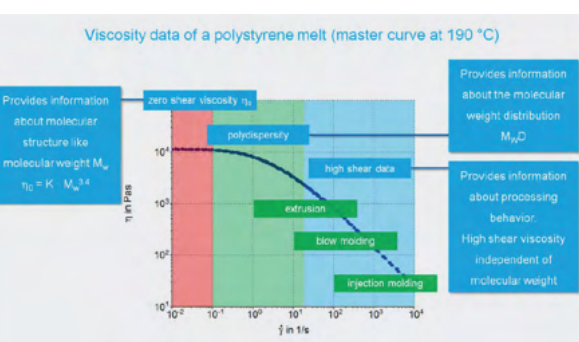


Figure 4: Shear rate depending viscosity of a polystyrene melt and typical applications.

Repetitive frequency sweep measurements over a narrow frequency range that capture the crossover point can therefore be used to detect thermal degradation causing changes to the MW and MWD.

Figure 5 shows how the crossover point (where $G' = G''$) shifts when the MW or the MWD change for an otherwise identical polymer melt.

As already mentioned, flow anomalies caused by the elasticity of polymer melts can lead to poor product quality in polymer processing applications such as extrusion. Figure 6 shows a comparison of storage modulus data as a function of the applied frequency for polyethylene samples with different Melt Flow Indices (MFI). The three PE samples were processed with a 16 mm parallel twin screw extruder under the same conditions.

At the end of the extruder barrel the melts were forced through a vertical rod capillary die with a diameter of 1 mm and an L/D ratio of 10. Die swell of the extrudate was measured with a laser micrometre. A die-swell of 0,5 mm, resulting in a total strand diameter of 1,5 mm, could be found for the PE with the highest MFI (~20) and the lowest molecular weight. As can be seen in Figure 6 the strand came out of the extrusion line as an even strand with no signs of surface defects.

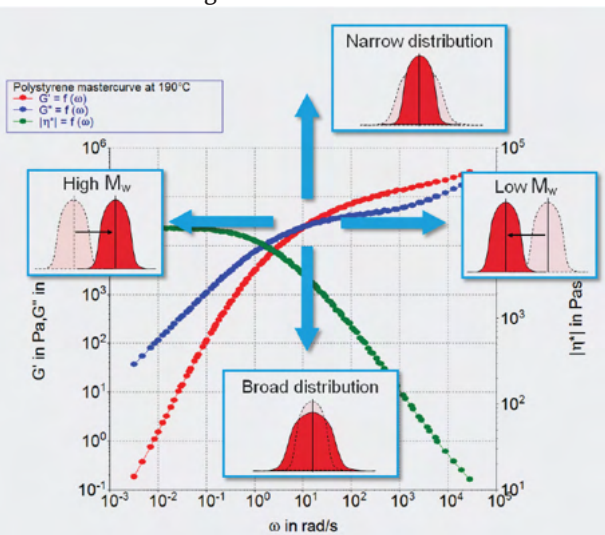


Figure 5: Storage modulus G' , loss modulus G'' and the complex viscosity η^* as a function of the angular frequency ω for a polystyrene melt at 190 °C.

The PE sample with the medium MFI (~ 2) already showed an uneven surface structure with a changing diameter. The PE sample with lowest MFI (~ 0.2) and the highest molecular weight showed clear signs of melt fracture under the same extrusion conditions used for the other two samples. When looking at the rheological data, one can see that the three samples clearly differ in terms of their elasticity, as represented by G' . Especially at the lowest frequency (10⁻² Hz), the values in G' differ in one or more orders of magnitude.

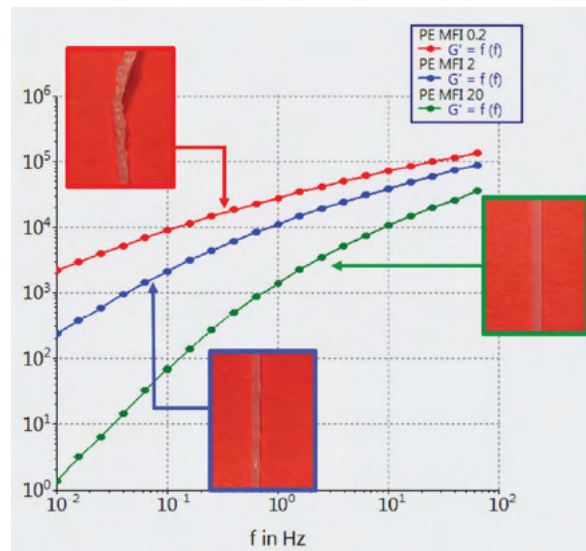


Figure 6: Storage modulus G' as a function of the angular frequency ω for polyethylene melts with different MFI at 190°C. The images show the extrusion strands that were prepared with the melts in a twin screw extrusion process.

The storage modulus is a very sensitive indicator of the elasticity incorporated by a high molecular weight tail.

Figure 7 shows the comparison of the results of three frequency sweeps performed on a low molecular weight LDPE and two blends of the same LDPE with a small weight fraction of a high molecular weight PE. In the low frequency range, G' shows clear differences for these three melts and even a small fraction of 1 wt% of high molecular weight PE can be detected. These small differences are usually not visible when performing Gel Permeation Chromatography (GPC) or similar techniques to determine the molecular weight distribution. Also, the MFI results performed with a capillary viscometer would not reveal any differences

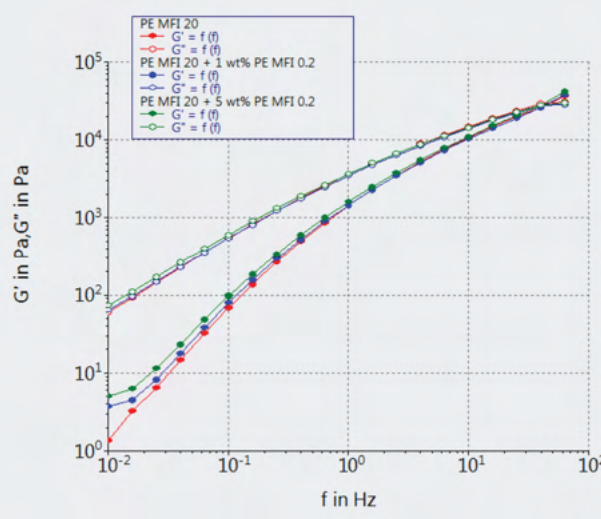


Figure 7: Storage modulus G' and loss modulus G'' as a function of the angular frequency ω for a low molecular weight polyethylene melt and two blends at 190°C.

between the three samples. The storage modulus data derived from oscillatory frequency sweep experiments is the most sensitive indicator of a high molecular weight tail in a polymer melt. Even small amounts of high molecular weight fraction can already cause flow anomalies that will lead to a poor quality of the final polymer strand.

Figure 5 shows rheological data acquired over an angular frequency range from below 10^{-2} rad/s to more than 10^4 rad/s.

In order to obtain rheological data over such a wide range, more than a single frequency sweep test is necessary. The low and high frequency regions are restricted by either time concerns (duration of a single oscillation) or the rheometer specifications (maximum frequency). The time-temperature superposition principle is then used to overcome these limitations.

Extending the measuring range

The time-temperature superposition principle

Usually between 2 and 4 orders of magnitude in frequency are covered in a single frequency sweep test. In order to extend the data range beyond the low- and

high-end frequencies, the Time-Temperature Superposition (TTS) principle can be applied. TTS uses the fact that temperature and frequency (time) have similar effects on the viscoelastic behaviour of polymer melts³. As a result, one can perform several frequency sweeps over a smaller range at different temperatures. After selecting one set of data (at one temperature) as a reference, the other results can be shifted towards the reference curve in order to generate a master curve. Using the TTS-principle, it is possible to obtain rheological data over a much wider frequency range compared to a single frequency sweep experiment. TTS works for many polymer melts and polymer blends but usually only over a limited temperature range⁴.

Figure 8a shows the results of several frequency sweep tests performed at different temperatures. The TTS principle was then applied, with 190 °C chosen as a reference temperature. The resulting master curve (Figure 8b) contains viscoelastic data over almost 8 orders of magnitude in frequency.

The master curve can be divided in three regions. At low frequencies, the sample is in the terminal region and the polymer melt behaves predominantly viscous. In the terminal region, material behaviour is governed by long molecule chain relaxation processes. Also, in the terminal region, G' and G'' typically have slopes of 2 and 1 in a double logarithmic plot.

At medium frequencies, a transition occurs with a crossover between G' and G'' . The viscoelastic behaviour in this range is strongly driven by the molecular weight distribution of the polymer. At the highest frequencies, the sample behaves predominantly elastic, with G' larger than G'' . Here the polymer's behaviour is governed by the fast relaxation motion of the shortest polymer chains.

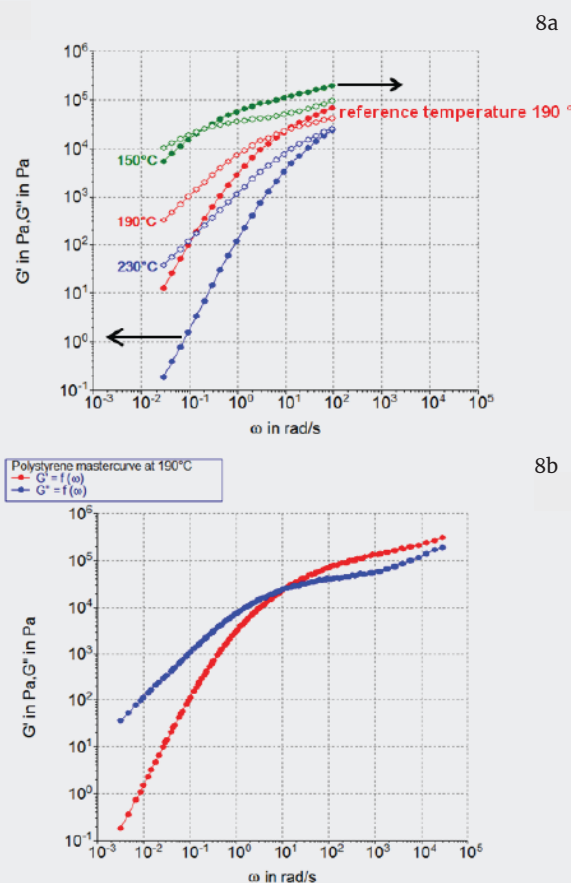


Figure 8: Application of the Time-Temperature-Superposition principle with a polystyrene melt.

In addition, G' and G'' data acquired over a wide frequency range can be used to calculate the molecular weight and molecular weight distribution for many linear thermoplastic homopolymers.

In order to perform this calculation, the tested frequency range must include data from the low frequency terminal region up to the end of the high frequency plateau region.

Investigating the final product properties

Dynamic Mechanical Thermal Analysis

Rotational rheometers can also be utilized to perform Dynamic Mechanical Thermal Analysis (DMTA) on solid, rectangular, or cylindrically shaped polymer specimens. During DMTA testing, a material is exposed to an oscillatory mechanical excitation while the

temperature is continuously changed. The obtained data is used to identify characteristic phase transitions, such as the glass transition or the occurrence of melting and/or crystallization within the polymer matrix. In addition, DMTA can be used to determine final product performance and to interrogate relevant application-based properties such as stiffness, brittleness, damping or impact resistance.

Figure 9 shows an example of a DMTA test with a semicrystalline polyetheretherketone (PEEK) sample, tested from below its glass transition to just below its melting temperature.

The test was performed using a special solid clamping tool for rotational rheometers^{5,6}. The rectangular specimen was prepared with a lab scale injection moulding system⁷. For rheological testing, the glass transition can be identified using different metrics. The most common metric uses the maximum in the loss modulus G'' , while the initial decrease in the storage modulus G' or the maximum in the $\tan\delta$ (G''/G') are also readily used to indicate glass transition. As can be seen in Figure 9, the maximum in G'' is located in the middle of a wider transition range, while the onset of the G' decrease is near the beginning of the transition and the maximum in $\tan\delta$ closer to the end of this range.

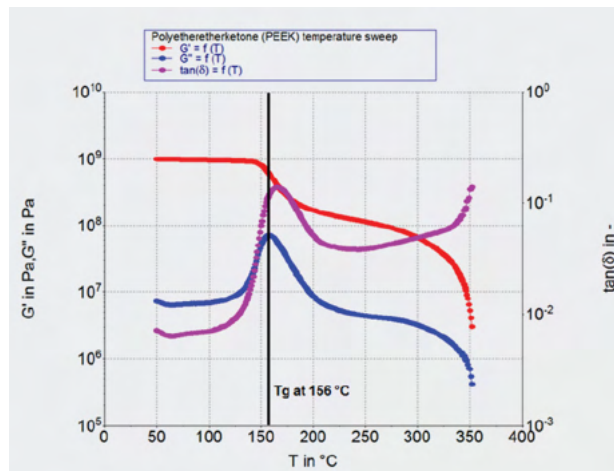


Figure 9: Storage modulus G' , loss modulus G'' and $\tan\delta$ as a function of temperature for a polyetheretherketone.

The generalized behaviour of a polymeric sample during a temperature sweep test is presented in Figure 10. All semicrystalline polymers transition from a glassy region at low temperatures to a rubbery plateau and eventually into the melt state at higher temperatures. The height of the step from the glassy region to the rubbery plateau depends on the degree of crystallinity of the polymer. As the degree of crystalline domains inside the polymer increases, the step height between the two regions will decrease.

Low molecular weight polymers do not exhibit a rubbery plateau. Once the glass transition is completed, the material becomes a soft melt and G' decreases with increasing temperature. Cross-linked polymers do not melt; instead, they remain in a rubbery state until thermal decomposition occurs.

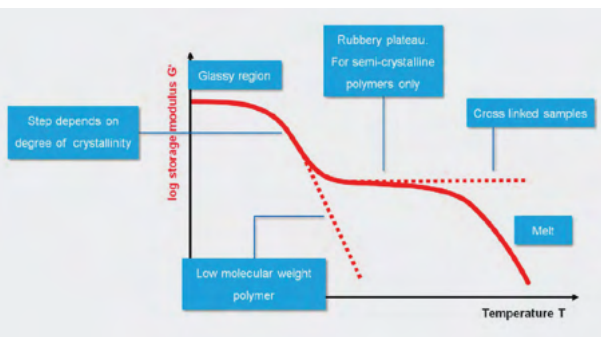


Figure 10: Generalized behavior of polymer sample in a DMTA test.

Extensional Testing

Besides rotation and oscillation, extension is the third main type of flow that can be investigated rheologically. Spraying and vessel filling are two examples of processes where extensional flows occur; however, they are not very common for polymer melts. Examples of processes where extensional flows occur and that are more closely related to polymer melts are film blowing, injection moulding, foam extrusion or fiber spinning. Figure 11 shows the transient extensional viscosity at different extensional deformation rates for two different polyethylene samples. The tests were performed with the Sentmanant Extensional Rheometer (SER) fixture for rotational rheometers⁸. The plot on the top presents the extensional behaviour of a non-branched high-density polyethylene (HDPE)

sample. No strain hardening was observed for this type of material. The plot on the bottom, however, shows the results of the same experiments, performed with a highly branched low-density polyethylene (LDPE) sample. For comparison, the red curves show the transient shear viscosities multiplied by three according to the Trouton ratio for uniaxial extension⁹. The shear viscosity data were obtained from rotational step experiments.

Unlike the linear HDPE sample, the extensional behaviour of the branched LDPE sample differed significantly from the behaviour observed in shear flow. During extensional testing, the LDPE sample displayed shear hardening behaviour, especially at higher deformation rates. Strain hardening behaviour can be beneficial for many polymer processing techniques such as film blowing or fiber spinning. Therefore, having a good understanding of the extensional behaviour of a polymeric material is crucial for optimizing its final product properties (behaviour that is left uncaptured by standard rotational rheological measurements).

Conclusion

Understanding the viscoelastic properties of a polymeric material is essential to optimize formulations and blends as well as to adapt a process to the properties of a given material and avoid problems caused by flow anomalies. Rheological tests performed with rotational rheometers can be utilized to investigate the viscoelastic behavior of polymers from the melt-state to the solid-state and everywhere in between. The obtained data can be used not only to optimize processing conditions and the final product performance, but also to establish structure property relationships. This is the reason why rheological tests are commonly used in analytics for polymeric fluids in industry as well as academia.

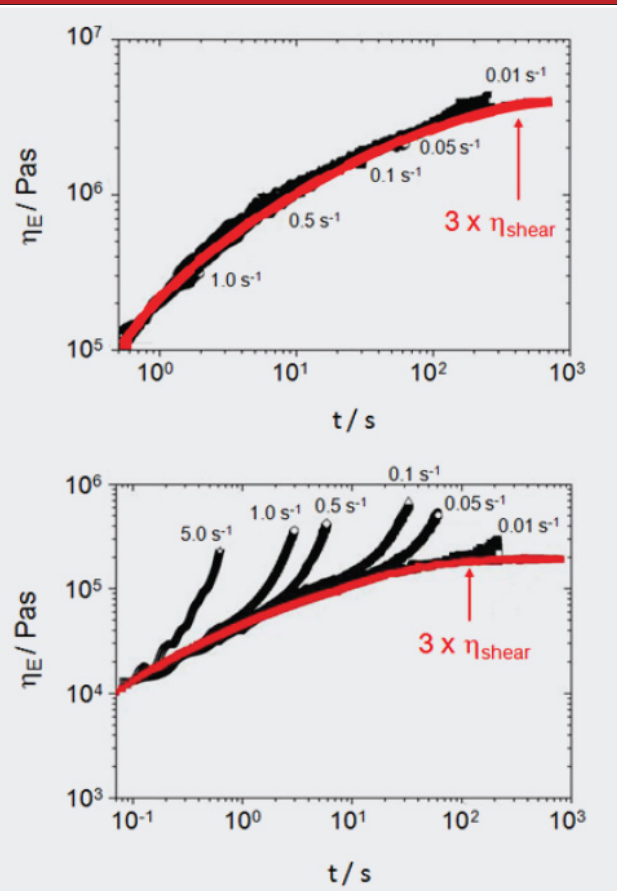


Figure 11. Extensional viscosity as a function of strain rate for a nonbranched HDPE (top) and highly branched LDPE (bottom). All tests were performed at 150 °C.

References

1. C.W. Macosko, *Rheology: Principles, Measurements, and Applications*, Wiley-VCH; New York (1994).
2. W.P. Cox and E.H. Merz, *Journal of Polymer Science*, 28, 619 (1958).
3. J.D. Ferry, *Viscoelastic Properties of Polymers*, 3rd ed., John Wiley & Sons, N.Y. (1980).
4. J. Dealy, D. Plazek, *Time-Temperature Superposition – A Users Guide*, *Rheology Bulletin*, 78(2), (2009).
5. C. Küchenmeister-Lehrheuer, K. Oldörp, F. Meyer, *Solids clamping tool for Dynamic Mechanical Analysis (DMTA) with HAAKE MARS rheometers*, Thermo Fisher Scientific Product Information P004 (2021).
6. C. Küchenmeister-Lehrheuer, F. Meyer, *Solids clamping tool for performing DMTA with rectangular specimens for HAAKE MARS iQ Rheometer Series with temperature chamber P077*
7. Thermo Scientific HAAKE MiniJet Pro, Thermo Fisher Scientific Specification Sheet (2014).
8. C. Küchenmeister-Lehrheuer, F. Meyer, *Sentmanat Extensional Rheometer (SER) for the Thermo Scientific HAAKE MARS Rheometers*, Thermo Fisher Scientific Product Information P019 (2023).
9. F. T. Trouton, *Proc. R. Soc. A77*, 426–440 (1906).





Water

Poison for Lithium-Ion Batteries

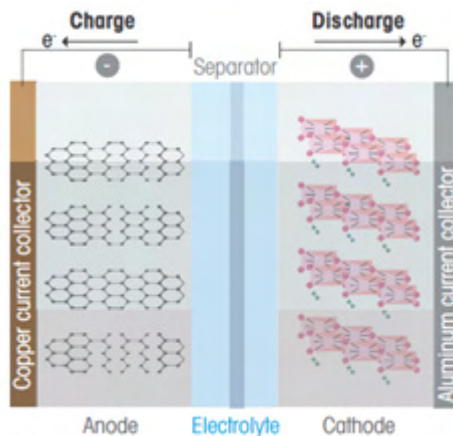
Water is poisonous to lithium-ion batteries. It reacts with the liquid electrolyte inside the battery to produce aggressive degradation products that greatly reduce performance.

Thorough testing for water in all functional components of a lithium-ion battery is therefore essential to ensure high quality.

Introduction

The ever-increasing market for portable electronic devices, together with the increasing pace of the electric vehicle (EV) revolution, has resulted in an equally large demand for rechargeable batteries¹. Lithium-ion batteries (LIBs) are state-of-the art in this technology and will presumably continue to be so, at least over the next several decades². This battery type exhibits a high energy density as it is light yet powerful, a good cycle durability as it can be charged and recharged without losing much energy per cycle, and a low self-discharge rate.

LIBs store energy that is released by an electrochemical reaction between the anode and the cathode material (Figure 1). Both cathode and anode contain positively charged lithium ions. During discharge, the oxidation reaction at the anode releases electrons and lithium cations. The electrons flow through an external wire to the cathode. To close the electric circuit, lithium cations flow through the liquid electrolyte and the separator to the cathode, where they recombine in a reduction reaction. During charging, the reactions at the electrodes are reversed and the lithium ions flow in the opposite direction. The lithium ions do not partake in the overall electrochemical reaction (Figure 1) and remain in their oxidation state.



Charge



Discharge

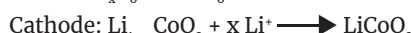


Figure 1: Charge and discharge reaction equations and a schematic of a lithium-ion battery with lithium cobalt oxide (LCO, LiCoO_2) as cathode.

The vast majority of LIBs use graphite ($\text{C}_6/\text{Li}_x \text{C}_6$) as anode material, which is abundantly available. The layered crystal structure of graphite allows the lithium cations to easily enter, also called lithium intercalation, and leave the electrode. Additionally, its low volume expansion during the charge/discharge cycle prevents

cracks and defects from forming in the solid material, which cause the battery to lose energy. Furthermore, graphite is a good electrical conductor. The electrons can flow through the graphite to the copper collector, to which the anode material is attached (Figure 1).

These desirable properties explain the widely accepted use of graphite as anode material. In contrast, there is significant room for improvement in cathodes, which are made of various materials, which depend on the final use of the battery. Lithium cobalt oxide (LCO, $\text{Li}_{1-x}\text{Co}_x\text{O}_2$) is the most commonly used cathode material. During charge, the cobalt is partially oxidized from Co(III) to Co(IV) and reduced to Co(III) again during discharge, respectively. The lithium ions balance the overall charge of the cathode and move either inside, or leave the material, in order to do so. However, although lithium cobalt oxide has a very high energy density, it also has its drawbacks. Cobalt is a rare, expensive resource, and cobalt reserves are mainly located in unstable regions². This concern led to the development of cobalt-saving lithium nickel manganese cobalt oxide (Li-NMC, $\text{Li}_a\text{Ni}_x\text{Mn}_y\text{Co}_z\text{O}_2$) cathodes. The drawback of Li-NMC cathodes is their slightly lower energy density. Both LCO and Li-NMC cathodes share the risk of oxygen production resulting in a runaway reaction and ultimately an explosion.

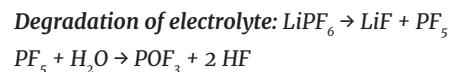
Lithium iron phosphate (LiFePO_4), another cathode material, is inherently safer but the trade-off is a lower energy density. It is therefore preferable for EV applications.

The anode and cathode are both soaked in a liquid electrolyte (Figure 1). Although lithium ions are principally not involved in the electrochemical reaction, it is important they are efficiently carried to the respective electrode.

The electrolyte is usually a mixture of organic carbonates and the electrolyte salt that increases the lithium-ion conductivity. Lithium hexafluorophosphate (LiPF_6) is the state-of-the-art electrolyte salt in such electrolytes. It dissolves well in organic carbonates, is

electrochemically stable and helps to conduct lithium cations. However, the use of LiPF_6 also comes with certain caveats. Traces of water in the electrolyte catalyse the formation of degradation products that can compromise the electrodes and the electrolyte itself (Equation 1). Amongst others, the electrical insulator, lithium fluoride (LiF), and hydrofluoric acid (HF) are formed³. Both substances lower the electrode's efficiency over time by either disturbing the lithium intercalation or the transport of electrons. HF can further lead to heat released due to degradation of the cathode, thereby risking a thermal runaway scenario³.

The bad influence on the battery's performance gives water its meaningful name: Battery poison.



Equation 1: Degradation reaction of the electrolyte. Water shifts the equilibrium to the right forming the electrical insulator LiF and PF_5 that further reacts to produce HF³.

Water – the most important QC parameter for battery manufacturers

Lithium-ion batteries exist in various forms for different applications. From mm-scale button cells for med tech applications to big battery packs in electric vehicles. In simple terms, manufacturers successively stack cathode and anode sheets, aluminium (cathode) or copper (anode) foil with active material on both sides and separate them with a polymer separator. These are brought together into a housing and the liquid electrolyte is added to produce the final battery. The water content of each component needs to be as low as possible.

Quality Control of Cathode and Anode

The best way to measure the water content of electrode sheets is the gas-extraction technique with coulometric Karl Fischer (KF) detection. The electrode sheets are cut into small flakes and ~2.5 g are filled into vials, placed onto the InMotion KF™ oven rack (Figure 2) and the method is started with OneClick™. The oven heats the electrode sample to 160 °C and a pre-dried stream of

nitrogen extracts and carries the vaporized water to the coulometric titration cell, where it is detected.

The analysis of anode and cathode sheets revealed water contents of 80.5 ppm and 103.2 ppm respectively with relative standard deviations of 1.5 and 1% (Table 1).

Quality Control of the Electrolyte

The measurement of the electrolyte is more challenging. The water content is very low (<15 ppm), it is highly hydrophilic, and commonly used organic carbonates like dimethyl, ethyl methyl and vinylene carbonate show side reactions with conventional methanol-based KF reagents. Low water content samples are most

accurately measured using coulometric KF titration. Small amounts of iodine are generated in-situ by a generator electrode.

The hydrophilicity of the electrolyte requires very careful sample handling. The syringes must be rinsed with the electrolyte prior to the injection. Using methanol-free KF reagents prevents side reactions and enables the solvent to be reused for several measurements.

Along with water, hydrofluoric acid (HF) – one of the detrimental degradation products of LiPF₆ – can be tested using an acid-base titration with sodium hydroxide as the titrant.

	Cathode Content (ppm)	Anode Content (ppm)	Electrolyte		
			Injected Samples	Sample Mass (g)	Content (ppm)
Blank 1	35.5 mg	44 mg	Standard	0.998	1004.0
Blank 2	31.5 mg	41 mg	1	1.935	8.2
Blank 3	31.3 mg	41 mg	2	1.749	11.5
1	102.4	81.20	3	2.250	12.6
2	104.1	81.70	4	1.803	14.0
3	104	80.20	5	1.996	10.4
4	102.3	79.00	Standard	1.017	1014.4
Mean	103.2	80.5	Mean		11.5
s	1	1.2	s		2.0
srel	1.00%	1.50%			

Table 1: Results of water content determination of lithium-ion battery cathode, anode and freshly opened electrolyte. The cathode and anode samples were analyzed using the gas-phase extraction technique with coulometric detection, whereas the electrolyte was analyzed using normal coulometric KF titration with direct injection.



Figure 2. C30S coulometric KF titrator with InMotion KF oven.

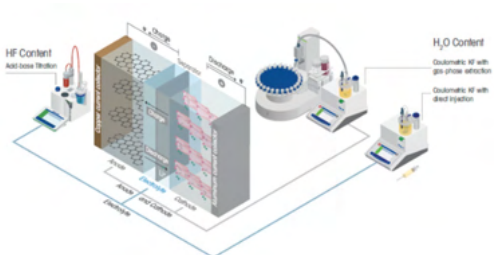


Figure 3. Left: Excellence T5 Titrator. Middle right: C30S coulometric KF titrator and InMotion KF oven; right: C30S coulometric KF titrator.

Conclusion

Water testing in LIBs is critical in QC as it reacts with the electrolyte to produce detrimental degradation products that reduce battery performance. Karl Fischer titration is the method of choice to measure water content in the main components – cathode, anode and electrolyte – before they are built into a battery housing.

References

1. Electric Vehicle Outlook 2020, www.about.bnef.com, visited 15.06.2020.
2. Azevedo M., Campagnol N., Hagenbuch T., Hoffman K., Lala A., Ramsbottom O., Lithium and cobalt – a tale of two commodities, McKinsey & Company, Metals and Mining, June 2018.
3. Stich M., Göttlinger M., Kurniawan M., Schmidt U., Bund A., *J. Phys. Chem.*, 2018, 122, 16, 8836–8842.





Battery Testing is revolutionising energy storage. Its development depends on meticulous research and precise experimentation.

In this interview, Dr. Anil Suryawanshi, Associate Technical Specialist at KPIT Technologies Ltd., Pune, talks in detail on the significance of gloveboxes in handling air-sensitive materials, and the best practices associated with utilizing these specialised environments.

Dr. Anil Suryawanshi is currently an Associate Technical Specialist at KPIT Technologies Ltd., Pune. He has dedicated the past eight years to the development of indigenous battery technology.

He is an Electrochemist and Material Scientist with expertise in novel functional materials/composites synthesis, characterizations, cell fabrication (from coin to pouch cells), testing, data analysis, and optimization for charge storage applications. His current research interests focus on the electrochemistry of alkali ion battery systems.



Battery Components

Q. Could you describe the process of assembling battery components inside a glove box and the key precautions necessary?

Glove box plays a very critical role in R&D of all types of rechargeable batteries such as lithium, sodium, solid state and metal batteries. Initial material development and cell fabrication parameters/steps require tuning inside the glove box. Assembling lithium or sodium-ion battery components within a glove box is a meticulous process. We must ensure a controlled environment, for maintaining the integrity of sensitive materials. Cell assembly involves several key components, including

cathode and anode electrodes, separator, electrolytes, and packaging cases for coin cell and polymer coated aluminium foil for pouch cell. For development of any cell chemistry, we need to first test in coin cells, optimize the electrode composition and electrolyte depending on the operating potential window and cell chemistry. Then we need to work on scaling up the capacity and performance on pouch/cylindrical or prismatic cell depending on requirement. For more details *I would like to explain cell assembly process for pouch cells.*

Interview

Pouch Cell Assembly Process involves the following steps

First, we have to punch the electrodes in the required sizes of cathode and anode from continuous coatings as per the size of interest and heat to remove the moisture from electrodes. *It will be good to use antechamber with heating arrangement to heat the electrodes to avoid further exposure to ambient conditions.* Make sure the moisture content in electrodes is <200 PPM. Mostly the PP, PE or tri-layer (PP/PE/PP) separators are used, based on cell chemistry. Like the electrode we need to remove moisture from separator by vacuum heating.

The next important step is stacking positive and negative electrodes with the help of separator, which can be done in the jelly form or Z stacking. As anode size is slightly larger than cathode, we need to use appropriate size of separator to avoid short circuiting in cells. For tab welding we can use ultrasonic tab welding machine to connect all positive/negative terminals together for external connections. After completion of cell sealing from 3 sides, we need to add electrolyte in adequate quantity and make sure the cell is getting completely soaked with electrolyte for utilization of all active materials. If we add excess quantity of electrolyte, it will add dead weight in the cell which will reduce the energy density of the cell. *With the help of degassing and diffusion chamber we can improve electrolyte soaking.* Final step in cell fabrication is vacuum sealing of pouch cell. *All these steps are carried inside a glovebox to avoid contamination or any exposure to moisture.*

Key Precautions:

Inert Atmosphere: The glove box must be purged with Ar gas to eliminate moisture and oxygen, which can degrade battery materials.

Personal Safety: Operators should wear protective gloves to prevent direct contact with potentially hazardous materials.

Contamination Prevention: All tools and materials should be cleaned and handled within the glove box to avoid contamination. While the glove box provides a controlled environment, it is also essential to consider

the potential for human error during assembly, which could compromise battery performance. Thus, rigorous training and adherence to protocols are vital for successful assembly.

Q. Could you explain how air-sensitive electrode material are handled within the glove box to maintain their integrity?

Air-sensitive sodium ion battery electrode materials require careful handling to maintain their integrity, primarily using glove boxes. These specialized environments minimize exposure to air, which can lead to degradation of the materials. The following sections outline the key aspects of handling these materials within glove boxes-

Glove Box Design and Functionality

Sealed Environment: Glove boxes are hermetically sealed to prevent air ingress, ensuring that sensitive materials remain isolated from oxygen and moisture.

Pressure Compensation: Advanced glove boxes incorporate pressure compensators to manage internal pressure changes without exposing the materials to air, thus preventing oxidation.

Handling Procedures

Argon (Ar) Atmosphere: Materials are often introduced into the glove box under an Ar atmosphere, which is inert and does not react with the electrode materials. **Nitrogen reacts with lithium metal, so argon gas is mostly used for operation of glove boxes.**

Controlled Access: The use of transitional openings and sealed gates allows for the safe transfer of materials in and out of the glove box without compromising the internal environment.

Material Stability Developments

Research and Development: Ongoing studies focus on improving the air stability of electrode materials through innovative design and synthesis methods.

While glove boxes provide a controlled environment for handling air-sensitive materials, the inherent challenges of maintaining such conditions highlight the need for continuous advancements in battery technology and material science.

Interview

Q. How do you prepare and handle electrolytes, especially considering critical factors like high flammability?

Researchers have developed various innovative strategies. These approaches focus on utilizing non-flammable solvents, enhancing electrolyte stability, and improving safety through material design.

Use non-reactive containers and tools, and ensure proper ventilation, preferably with the help of purging system included in the glove box. Store the electrolyte in airtight, sealed containers under inert gas and away from heat sources or open flames. Handle small quantities to minimize risks and use spill kits to manage leaks or accidents promptly. *It is recommended to operate glove box under purging condition, in case there is exposure to too much solvent vapours or contamination, to improve the catalyst life, which is the heart of glove box.*

Q. How do you analyse battery performance like voltage, capacity, internal resistance etc?

Analysing battery performance involves evaluating key parameters such as voltage, capacity, and internal resistance through various methodologies. These assessments are crucial for understanding battery performance health and efficiency, and several innovative techniques have been developed to facilitate this analysis.

Battery performance is analysed through several key tests-

Voltage is measured directly using a multimeter or battery tester to ensure it falls within the expected range. Firstly, we need to optimise the stable operating potential window for battery chemistry. Which we can do with the help of cyclic voltammetry. The cycle life of the battery depends on operating potential of battery. Overcharge or over discharge of any battery cycle hampers the cycle life as well as safety.

Capacity is evaluated through charge/discharge cycling using a battery cycler, measuring the total energy stored and delivered (typically in mAh or Wh). For testing

material capacity, we need to fabricate half cells with the help of metal anode (Li/Na).

Internal resistance is assessed using electrochemical impedance spectroscopy (EIS) or by measuring voltage drop under load; this indicates the cell's ability to conduct current efficiently. It's very important to study change in internal resistance of battery with SOC which we can do with the help of HPPC measurements. Heat generation in the battery is dependent on how the internal resistance of cell chemistry is changing with SOC.

Contamination and Safety

Q. What are the different types of contaminants and how do each of them affect the quality of performance of battery components?

Contaminants in batteries can include moisture, metal particles, organic residues, and dust or particulate matter, each affecting performance uniquely:

Moisture reacts with electrolyte salts (e.g., LiPF₆ or NaPF₆), producing HF and causing degradation of electrodes, reduced capacity, and increased self-discharge. Also few materials are moisture sensitive which degrade/ change phase after getting exposed to moisture.

Metal Particles may cause internal short circuits, leading to capacity loss, thermal runaway, or catastrophic failure. One more degradation mechanism caused by metallic impurity is electrolyte degradation due to catalytic activity of metal particles on the surface of cathode or anode. Which increases thickness of SEI and CEI.

Organic Residues from adhesives or processing chemicals can interfere with electrochemical reactions, reducing efficiency and increasing resistance.

Dust or Particulates block active sites on electrodes, hinder ion transport, and can lead to inconsistent performance.

Proper manufacturing controls and a clean environment minimize these contaminants, ensuring battery reliability and safety.

Interview

Q. How do you ensure that the battery components are free of contaminations before and after placing in the glove box?

To ensure battery components are contamination-free, clean all parts and tools thoroughly using solvents like isopropyl alcohol before introducing them to the glove box. Use a vacuum oven to dry moisture-sensitive components and materials. Inside the glove box, maintain low oxygen (<1 ppm) and humidity levels (<1 ppm). Regularly purge the glove box and monitor its atmosphere with sensors. After assembly, inspect components for visible contaminants, and store them in clean, sealed containers to prevent post-processing contamination.

Q. Could you delineate safety hazards associated in handling battery components and highlight the precautionary steps you follow?

Safety hazards in handling battery components include **chemical exposure** (toxic or corrosive materials), **flammability** (organic solvents or electrodes), **electrical hazards** (short circuits), and **mechanical risks** (sharp edges or mishandling). Precautions include wearing PPE (gloves, goggles, lab coats), working in a ventilated and dry environment, using tools rated for battery work, avoiding open flames, and handling materials in inert atmospheres like a glove box. Ensure proper storage of flammable and reactive materials and have emergency equipment like spill kits and fire extinguishers readily available. Training and adherence to safety protocols are essential.

Q. How do you safely integrate the glove box with external battery testing equipment like impedance analysers, potentiostats etc?

To safely integrate a glove box with external battery testing equipment, use **air-tight feedthroughs** or ports to pass electrical connections without compromising the glove box atmosphere. Ensure all cables are properly insulated and sealed. Position the testing equipment outside the glove box to minimize contamination risks. Maintain the glove box's inert environment by monitoring and purging regularly. Verify that the connection process does not introduce moisture or oxygen and test the integrity of the seals before starting

experiments. Follow equipment-specific grounding and safety protocols to prevent electrical hazards.

Performance and Impact

Q. What are the specific considerations for a glove box for battery testing applications?

For battery testing applications, a glove box must maintain ultra-low oxygen (<1 ppm) and humidity levels (<1 ppm) to protect sensitive materials. It should feature air-tight seals, feedthroughs for electrical connections, and compatibility with flammable materials (e.g., fire suppression systems). *The box should have a controlled atmosphere with inert gas (argon or nitrogen), efficient gas purging, and a monitoring system for environmental conditions. Additionally, it should include anti-static features, ergonomic design for handling, and proper lighting for visibility. Regular maintenance ensures consistent performance and contamination prevention.*

Q. What are the benefits of integrating the glove box with in-situ analytical techniques like XRD, electrochemical impedance spectroscopy, etc?

Integrating the glove box with in-situ analytical techniques like XRD and electrochemical impedance spectroscopy (EIS) offers several benefits:

It allows for real-time monitoring of battery materials and electrochemical processes under controlled, oxygen- and moisture-free conditions. *This integration enables precise analysis of phase changes, structural stability, and impedance variations during cycling*, leading to better understanding of material behaviour, improved performance optimization, and accelerated development of battery technologies. It also minimizes contamination risks and ensures accurate, reliable data.

Q. How do you perform degradation tests of battery components in the glove box to understand material performance?

To perform degradation tests of battery components in the glove box, first prepare the components (electrodes, electrolyte) in a controlled inert atmosphere. Assemble the battery in the glove box and subject it to

Interview

charge/discharge cycling under specified conditions, monitoring parameters like capacity fade, voltage profiles, and internal resistance. Perform electrochemical impedance spectroscopy (EIS) or cyclic voltammetry (CV) to analyse material stability. Regularly assess structural integrity using techniques like X-ray diffraction (XRD) or scanning electron microscopy (SEM). These tests help identify degradation mechanisms such as SEI layer growth, electrode pulverization, or electrolyte breakdown. Also glove box is very helpful to do the postmortem analysis of cell chemistry. Opening any battery chemistry with proper safety tools helps to understand degradation mechanism in batteries. The degradation triggered from cathode, anode and electrolyte we can try to find out possible degradation mechanism by characterisation of cathode, anode electrodes as well as if required electrolyte.

Q. Comment on the importance of glove box during the charging and discharging tests. How do you monitor these conditions?

The glove box is crucial during charging and discharging tests to maintain a controlled, inert atmosphere, preventing moisture and oxygen from degrading sensitive battery components. Such type of activity we need to do for air sensitive and moisture sensitive cell chemistries such as Li/ Na metal batteries, solid state batteries as well as for anode free batteries. *Inside the glove box, the battery is cycled while ensuring optimal conditions for accurate performance data. Conditions like temperature, humidity, and gas composition (e.g., low oxygen and moisture) are continuously monitored using sensors.* Data from charge/discharge cyclers and electrochemical analysers track parameters like voltage, current, capacity, and internal resistance. This controlled environment ensures reliable, reproducible results without contamination.

Future prospects

Q. Could you discuss emerging trends in battery research and how the glove box would evolve to support these advancements?

Emerging trends in battery research, such as solid-state

batteries, metal batteries, anode free batteries, sodium-ion batteries, and advanced electrolyte formulations, are pushing the boundaries of energy storage technology. These innovations require increasingly precise control over the environment to prevent degradation from moisture and oxygen. Glove boxes will evolve to support these advancements by incorporating advanced gas and humidity control systems, automated in-situ monitoring tools (such as integrated spectroscopic and electrochemical analysis), and high-throughput testing capabilities for rapid material screening. Additionally, future glove boxes may feature enhanced safety features for handling more reactive materials and support real-time data acquisition to optimize battery performance and accelerate the development of next-generation energy storage solutions.

Q. Can you remark on the use of glove boxes in high-throughput battery testing for rapid screening for new materials and cell designs?

Glove boxes are essential for high-throughput battery designing, development and prototyping of any chemistry. Glove box provides a controlled, contaminant-free environment crucial for screening new materials as well different types of cell designs. These systems enable the assembly and testing of numerous battery cells in parallel, ensuring consistent conditions (e.g., low oxygen and moisture) across all samples. *By integrating with automated equipment and advanced analytical tools, glove boxes facilitate rapid charging/discharging cycles, electrochemical analysis, and material characterization as well as to find out degradation mechanisms in batteries.* This setup allows researchers to efficiently evaluate the performance, stability, and scalability of new materials and designs, significantly accelerating the discovery and optimization of next-generation battery technologies.

Automatic Detection of the Thermal Degradation of a Polymer

Rheological Characterisation of Polymers using the Thermo Scientific HAAKE MARS Rheometer

There is direct correlation between properties of a polymer and its chemical behaviour. It is established that the crossover frequency is linked to the molecular weight, while the crossover modulus is directly related to the polydispersity index (PI). To achieve the desired material characteristics, precise control over such parameters is required. In this aspect, rheological analysis provides a valuable approach to characterize parameters like frequency sweep measurements.

This study accentuates the advantages of the Thermo Scientific HAAKE MARS Rheometer for polymer analysis.

Keywords or phrases: Rheometer, polymer analysis, polydispersity, Thermo Scientific HAAKE MARS Rheometer

Introduction

Similar to any other material, the properties of polymeric materials are closely linked to their chemical nature. What makes polymers so different from low-molecular-weight substances is the huge influence of their molecular weight (MW) and their molecular weight distribution (MWD) on their macroscopic behaviour.

Without changing its chemical nature, we can e.g. "select" the rigidity or elasticity of a polymeric material just by varying the parameters of the polymerization process.

Thus, to make a polymer with the desired properties we have to be able to quickly determine the right moment to stop the polymerization process in order to always get the same MW and MWD. Also, these two parameters can be used to decide whether materials delivered meet the specifications or not.

Application Showcase

One widely accepted method makes use of the fact that the crossover frequency determined with a frequency sweep (Figure 1) depends on the MW of a polymer, whereas the crossover modulus is related to its MWD.

From the crossover modulus the polydispersity-index (PI) can easily be calculated:

$$PI = 100.000 / \text{Crossover Modulus [Pa]}$$

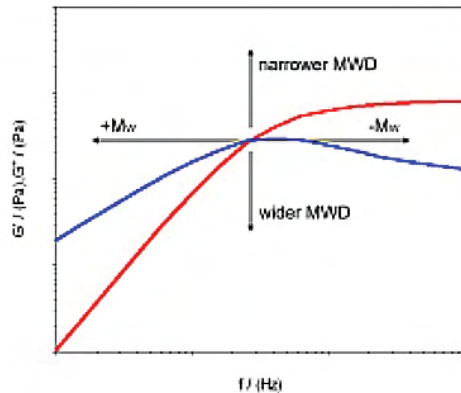


Figure 1. Schematic crossover dependency on MW and MWD

The Thermo Scientific HAAKE MARS is a high-end rheometer, which has a number of important advantages for polymer analysis.

Amongst them is the sensitive normal force sensor, which allows the measurement of forces down to 0.01 N. In combination with the precise lift control this is a great tool to ensure the reproducible loading and axial relaxation of samples.

Another unique feature of the HAAKE MARS is the Controlled-Environment-Chamber (CTC). Its powerful combination of convection and radiation heating guarantees the quick adjustment of temperature and low temperature gradients in the sample.

Measurements

For these measurements very narrowly, distributed polybutadienes have been selected. Samples with a diameter of 25 mm were cut from a sheet of approximately 2 mm thickness. While the CTC was preheating to 190 °C in its parking position, the sample

was put into the 25 mm parallel plate geometry of the HAAKE MARS, and the gap was closed with a defined axial force to have the same starting conditions for different samples. With these preparations it was possible to run frequency sweeps in a very reproducible way as can be seen in Figure 2.

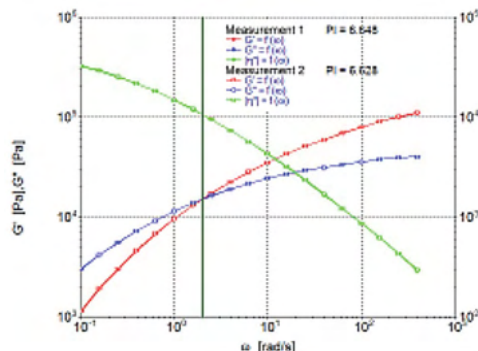


Figure 2: The crossover of the storage modulus (red) and the loss modulus (blue) during a frequency sweep is related to MW and MWD. From the cross-over modulus, here 15000 Pa, the so-called polydispersity-index can be calculated, here 6.6. Due to the good reproducibility, the 2 measurements are barely distinguishable.

The resulting curves were practically identical, and the PI values calculated differed only about 0.3 %. These measurements were performed under laboratory conditions, so the whole procedure before starting the measurements, i.e. sample loading, closing of the geometry, was the same in all cases. In working environments where this is not possible, it is especially important to know, whether the polymer regarded is stable e.g. against oxidation at elevated temperatures.

Otherwise, different results can simply be based on different times it took to start the measurements.

This possible degradation of a polymeric sample can be detected using the HAAKE MARS. For that purpose, a different polymer sample was prepared and loaded into the rheometer at 190 °C as described above.

After equilibration, 15 identical frequency sweeps were done over a time span of 60 min. From earlier measurements we knew roughly, where the crossover could be observed.

Application Showcase

any input from the operator's side once the sample has been loaded.

As shown in Figure 3, the G' and G'' curves shift to lower values the longer the sample is exposed to the 190 °C inside the CTC. Subsequently the crossover shifts to lower moduli and higher frequencies (Figure 4), indicating a decrease of the average molecular weight of the polymeric material tested and a broadening of its molecular weight distribution.

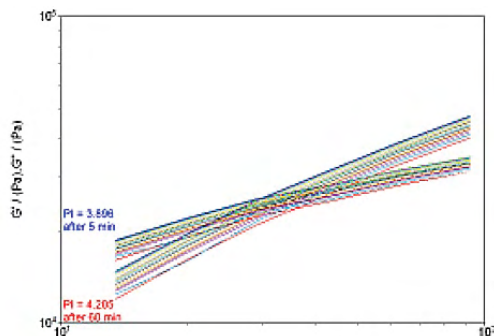


Figure 3: Polymer sample kept for 60 min in the rheometer at 190 °C while running 15 frequency sweeps. From run to run the curves of both G' and G'' shift to lower values (from blue to red).

Expressed in terms of the polydispersity- index we see an increase from 3.9 to 4.2. For usual technical polymers with a broader distribution any kind of degradation would initially affect the higher molecular weights and lead to a narrower distribution.

Since the polybutadienes used for this study had a very narrow distribution, degradation leads to an increase of smaller molecular weights and thus broadens the molecular weight distribution.

The data evaluation from this test clearly shows that indeed a thermal degradation of the polymer has occurred.

Summary

Using the normal force-controlled sample loading for polymer samples of an unknown thickness, the HAAKE MARS equipped with the CTC shows perfectly reproducible results from frequency sweep measurements.

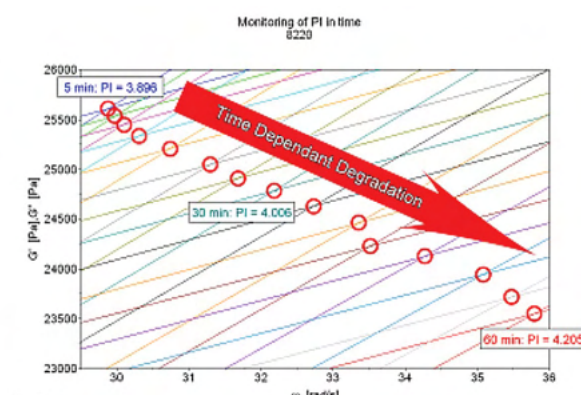


Figure 4: During 60 min at 190 °C the crossover shifts to higher frequencies and lower moduli showing the decrease of MW and the broadening of MWD.

Having seen this great reproducibility any decrease of the crossover modulus and increase of the crossover frequency can be solely attributed to a thermal degradation of the polymer sample tested. The possibility to preheat the CTC in its parking position and the selection of a suitable frequency range minimized the time needed for the measurement. The method described enables a very cost-effective polymer analysis and is also suitable whenever a quick answer is needed.

With the capabilities of the HAAKE RheoWin to run a fully automated test method, the HAAKE MARS equipped with the Controlled Test Chamber (CTC) is the perfect tool to determine if a polymer shows thermal degradation in a very time saving and cost saving way. In case the rheological properties of an oxygen-sensitive polymer have to be measured at higher temperatures over a longer time, the CTC can be flushed with nitrogen instead of air to exclude the damaging influence of the otherwise unavoidable oxygen.

ThermoFisher
SCIENTIFIC



HAAKE MARS
Rheometer with
Controlled-Environment-Chamber

100 MHz Benchtop NMR Spectrometer

The top-of-the-line benchtop NMR

- › The highest field available
- › Easy-to-use and
- › low maintenance



Pulsed Field Gradients (PFGs)

1 Enhance solvent suppression routines

Solvent suppression routines are used to suppress strong signals, typically solvent, in the spectrum. Gradient-based approaches, such as WET, often yield a higher-quality suppression signal.

2 Speed up 2D NMR data acquisition

The advantage of using gradient-based pulse programs to acquire your 2D NMR spectra is that data can typically be acquired faster and with fewer artifacts than conventional sequences.

Includes sequences such as

WET 1D-CPMG-filter-WET gCOSY gTOCSY
gHSQC gHSQC-ME gHMQC gHMBC

 **nanalysis**™

Operating frequency

100MHz (2.35T)

Nuclei

$^1\text{H}/^{19}\text{F}/^{13}\text{C}$, $^1\text{H}/^{19}\text{F}/^{31}\text{P}$

Sample

Standard 5mm NMR tubes

Operating Temperature

18 – 26 °C

Connectivity

Ethernet/WiFi, USB, Serial, HDMI

Hydrofluoric Acid Content of Lithium-ion Battery Electrolyte

Potentiometric Titration in the Mettler Toledo Titration Excellence T5 To Determine HF Content

Lithium-ion batteries (LIB) are commonly used for portable electronic devices and electric vehicles. They are growing in popularity because of their high energy density. The lithium-ion battery stores energy that is released by an electrochemical reaction between the anode and the cathode material. Both the anode and the cathode contain positively charged lithium ions. During discharge, the oxidation reaction at the anode produces electrons and lithium cations. The electrons flow through an external wire to the cathode. To complete the electric circuit, lithium cations, flow through the electrolyte to the cathode where they recombine with the electron in a reduction reaction. Although the lithium ions formally do not partake in the electrochemical reaction, it is important that they are efficiently carried to the respective electrode by the electrolyte.

Keywords or phrases: Lithium- ion, electrolyte, hydrofluoric acid, titration, battery, lithium, Mettler Toledo

Introduction

The electrolyte is usually composed of the electrolyte salt and a number of additives (e.g. organic carbonates). Lithium hexafluorophosphate LiPF_6 is the most frequently used electrolyte salt in LIB electrolytes. It dissolves well in organic carbonates, is electrochemically stable and helps to conduct lithium cations. However, the use of LiPF_6 also brings up a problem. It is not stable against hydrolysis. Traces of water in the electrolyte lead to the formation of hydrofluoric acid HF, which is considered as battery poison destroying the electrodes and lowering the capacity. Therefore, the amount of HF in the

Application Showcase

lithium-ion battery electrolyte should be as low as possible. The HF content serves as a quality indicator and is listed in the specification of the electrolyte.

This application note describes a method to determine the hydrofluoric acid content in a lithium-ion battery electrolyte by an aqueous acid-base titration with potentiometric indication.

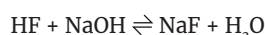
Sample Preparation and Procedures

Add approximately 40 mL of deionized water into a 100 mL titration beaker and place the beaker on the balance.

Tare the balance and add ca. 3 g of the electrolyte using a syringe.

Then place the beaker on the InMotion autosampler rack and start method as shown in Table 2.

Chemistry



Chemicals

Titrant: Aq. sodium hydroxide, NaOH, $c(\text{NaOH}) = 0.01 \text{ mol/L}$.

Sample: Lithium hexafluorophosphate solution in ethylene carbonate and ethyl methyl carbonate, 1.0 M, LiPF₆ in EC/EMC=50/50 (v/v), battery grade

Analyte: Hydrofluoric acid, HF, $M = 20.01 \text{ g/mol}$, $z = 1$.

Auxiliary Reagents: deionized water.

Standard: Potassium hydrogen phthalate, C₈H₅KO₄, $M = 204.22 \text{ g/mol}$, $z = 1$

Instruments and Accessories

- Titration Excellence T5
- InMotion flex 100 mL
- Burette DV1010 10 mL
- Compact Stirrer
- DGi111-SC or DGi115-SC electrode

➤ Excellence balance XPR603S Delta Range

Results

	Sample Size (g)	R1: Content (ppm)
1	2.8542	75.02
2	3.1214	76.78
3	2.897	78.62
4	2.7795	75.61
5	2.8144	76.52
6	3.2041	76.97
Mean		76.59
s		1.24
srel		1.62%

The results show a good repeatability with a relative standard deviation of 1.7%. The results are listed in chronological order. The inexistence of a trend towards increasing values indicates that the hydrolysis during the sample handling is negligible.

Measured Values

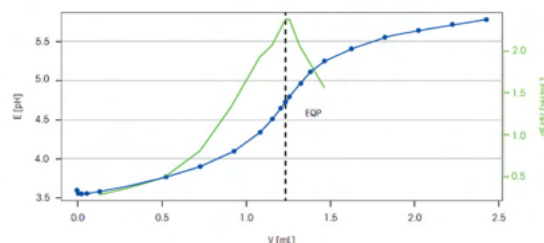


Figure 1: Titration curve (blue) and the first derivative of the titration curve (green) of sample 6/6.

Application Showcase

Method

Sample		Evaluation and Recognition	
Sample Type	Sample	Procedure	Standard
Number of IDs	1	Threshold	1.5 pH/mL
ID 1	Electrolyte	Tendency	Positive
Entry type	Weight	Ranges	0
Lower Limit	0	Add. EQP criteria	No
Upper Limit	5 g	Termination	
Density	1 g/mL	At Vmax	5 mL
Correction Factor	1	At potential	No
Temperature	25.0 °C	At slope	No
Titrator reader	None	After number of recognised EQPs	Yes
Number of sample factors	0	Number of EQPs	1
Titration stand		Combined Termination Criteria	No
Type	InMotion T/Tower A	Condition	No
Titration Stand	InMotion T/1A	Calculation R1	
Head Position	Sample	Result	Content
Stir		Result Unit	ppm
Speed	30%	Formula	$R1=Q*C/m$
Duration	5 s	Constant C	$C=M*1000/z$
Titration (EQP)1		M	M[Hydrofluoric acid]
Titrant		Decimal Places	3
Tirant	NaOH	Result Limits	No
Concentration	0.01 mol/L	Extra Statistical Functions	No
Sensor		Send to Buffer	No
Type	pH	Write to Smart Tag	None
Sensor	DGi111-SC	Condition	No
Unit	mV	Rinse	
Temperature Acquisition		Auxiliary Reagent	Water
Temperature Measurement	No	Rinse Cycles	1
Stir		Vol. per cycle	10 mL
Speed	30%	Position	Current Position
Predispense		Drain	No
Mode	None	Condition	No
Wait time	0 s	End of Sample	
Control		Park	
Control	Cautious	Titration Stand	InMotion T/1A
Mode	Acid/Base	Position	Condition Beaker
Titrant Addition	Dynamic	Condition	No
dE (set value)	10 mV	Record	
dV (min)	0.005 mL	Report Template	Titration Report
dV (max)	0.2 mL		
Mode	Equilibrium controlled		
dE (set value)	0.5 mV		
dt	2 s		
t (min)	3 s		
t (max)	30 s		

Table 2: Experimental Method

Application Showcase

t (s)	V (mL)	E (pH)	dE/dV (mV/mL)
0	0	3.586	n/a
3	0.005	3.553	n/a
6	0.01	3.55	n/a
9	0.0225	3.549	n/a
12	0.0535	3.554	n/a
17	0.131	3.58	0.3
23	0.325	3.66	0.38
30	0.525	3.766	0.51
37	0.725	390.10%	0.82
47	0.925	4.097	1.38
60	1.083	4.343	1.93
72	1.153	4.505	2.07
86	1.204	4.646	2.25
EQP	1.23252	4.726	2.37
100	1.2555	4.7	2.37
118	1.318	4.964	2.05
138	1.3805	5.113	1.86
159	1.4645	5.25	1.86
181	1.623	540.80%	n/a
206	1.823	555.50%	n/a
222	2.023	5.643	n/a
238	2.223	5.723	n/a
251	2.423	5.783	n/a

Conclusion

LiPF_6 hydrolyses slowly in aqueous solutions, while it is hydrolysing faster in organic solutions with traces of water¹. Thus, the titration is conveniently performed in water using aqueous NaOH as titrant.

To prevent the further formation hydrofluoric acid by hydrolysis, the sample should be titrated readily.

This method was only tested on the presented sample. The compositions of Lithium-ion battery electrolytes vary, and some electrolytes may contain additives that hydrolyse to form of hydrofluoric acid very quickly. For such samples, it may be necessary to strictly work in non-aqueous conditions.

The titre of aq. 0.01 M sodium hydroxide solution is determined using potassium hydrogen phthalate (KHP) as the primary standard. As the optimum amount of standard per measurement is very low (5 mg), a

5 mg/mL aq. KHP standard solution is prepared.

After every sample, the electrode, stirrer and tubing are rinsed with deionized water.

The titrations are performed in plastic beakers as HF is able to etch glass.

Waste Disposal and Safety Measures

Although the hydrofluoric acid content of the electrolyte is quite low, every contact with skin or eyes should be prevented. Use gloves, safety goggles and a lab coat. Work in a fume hood. After the titration, all solutions are neutralized and disposed as aqueous waste.

Reference

1. Stich M., Göttlinger M., Kurniawan M., Schmidt U., Bund A., *J. Phys. Chem.*, 2018, 122, 16, 8836–8842.

Titrator Excellence T5



Evaluation of Recycled Polymers by Thermal Analysis

DSC and TGA measurements on PET moulded products using the Hitachi High-Sensitivity Differential Scanning Calorimeter and Simultaneous Thermogravimetric Analyzer

Recycling plastics induces unwanted changes in material properties. These alterations in glass transition temperature, crystallization behaviour, decomposition temperature etc, significantly impact the performance, quality and processability of recycled polymers. Thermal analysis of recycled polymers is vital for quality assessment for further processing, depending on their intended application.

This application evaluates the differences in thermophysical properties of three types of PET molded products with different mixing ratios of recycled PET and virgin PET by the DSC and the Sample Observation TG measurements.

Keywords or phrases: Polymer, recycling, thermal analysis, Differential Scanning Calorimeter, Thermogravimetric Analysis, glass transition, crystallization, Hitachi.

Introduction

Efforts to recycle plastic products are becoming more and more active in many countries for the purpose of effective use of resources and prevention of environmental pollution. Recycling includes material recycling, in which crushed materials are melted and molded after removal of foreign substances, and chemical recycling, in which materials are chemically decomposed and repolymerized. There are concerns that these processes may cause impurities, changes in molecular weight, differences in crystal structure, etc., which may alter the properties of the virgin product¹. Thermal properties such as glass transition temperature, melting temperature, crystallization temperature, and decomposition temperature may vary, and thermal analysis can be used to select materials suitable for final products and to study processing temperature conditions.

Application Showcase

This report introduces an example of evaluating the differences in thermophysical properties of three types of PET molded products with different mixing ratios of recycled PET and virgin PET by the DSC and the Sample Observation TG measurements ^{2,3}.

Measurements

Three types of commercially available PET molded products with recycled PET content of 0, 60, and 90 % were used as samples for measurements.

DSC measurements were performed using the Hitachi DSC7000X High-Sensitivity Differential Scanning Calorimeter for constant rate heating and cooling measurements and isothermal crystallization measurements. In the constant rate heating and cooling measurement, the first heating, cooling, and second heating were scanned repeatedly at 10 °C/min in the temperature range of 25 to 280 °C. In the isothermal crystallization measurement, the crystallization was measured by quenching the specimen from 280 °C to 220 °C and then holding it for 60 min.

TG measurement was performed using the Hitachi STA200RV Simultaneous Thermogravimetric Analyzer equipped with the RVST0010 Sample Observation System Option. Measurements were performed over a temperature range of 25 to 600 °C at 20 °C/min under dry air atmosphere. In addition to measuring the mass change, an attempt is made to quantitatively analyze the color change by performing L*a*b* color space analysis^{4,5} of the sample observation images from melting to the initial decomposition process.

Measurement Results

Constant rate heating and cooling measurements

Figure 1 shows the results of constant rate heating measurement by DSC. In order to compare the effect of recycled PET content on thermal properties, the thermal history of each sample was reset by the first heating, and the results of the second heating after cooling are shown here. For each sample, an endothermic shift due to glass

transition is observed around 80 °C, and an endothermic peak due to melting is observed around 250 °C. The start and end temperatures of the glass transition are shown in Figure 1. The glass transition temperature (T_{ig}) is the highest for the recycled PET content of 0 %. And T_{ig} lowered with an increase in the content of the recycled PET.

Also, the temperature range of the transition region from the start temperature to the end temperature of the glass transition was 11.4 °C for 0 %, 12.8 °C for 60 %, and 13.7 °C for 90 %. T_{ig} tends to become higher with increasing molecular weight and to become wider with increasing molecular weight distribution. In this measurement, it is assumed that the molecular weight and T_{ig} shifted lower by increasing the content of the recycled PET and the broadening of the molecular weight distribution is described to an expanded temperature range of transition region.

Similarly, there are differences in the melting peaks, which may be due to the effect of molecular weight and molecular weight distribution. The melting temperature decreases with increasing recycled PET content, and the width of the peaks becomes wider, and there is a tendency for double peaks. Figure 2 shows the integral curves of these melting peaks. For the samples with 60 % and 90 % recycled PET content, melting starts around 200 °C. It is suggested that this is due to the melting of components that were changed to low molecular weight in the process of recycling.

By analyzing the heat of melting, ΔH_m , the degree of crystallinity of the samples can be compared. From Figure 1, it is found that the heat of melting decreases with decreasing content of recycled PET. This phenomenon means that more amount of crystallized components formed during the 10 °C/min cooling after the 1st heating.

Application Showcase

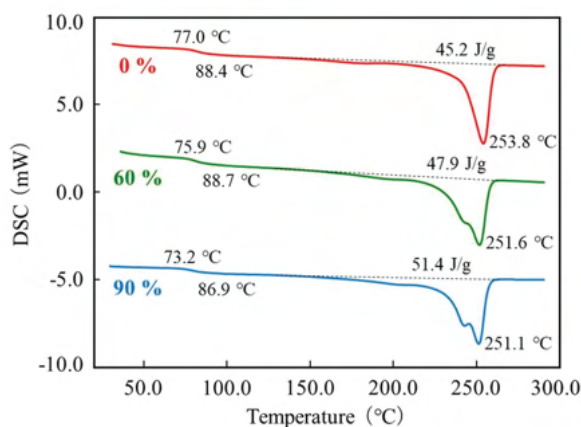


Figure 1: DSC curves of PET after 10 °C/min cooling

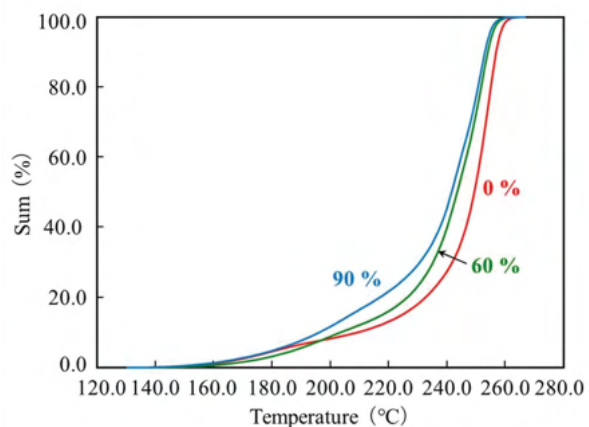


Figure 2: Integral curves of melting peak for PET

Crystallization tends to progress easily the components that form the nucleus of the crystal are included. Impurities mixed in the recycling process may remain in the recycled materials. It is thought that the higher the recycled material contains, the higher the heat of melting of the crystals as the impurities act as a nucleus to promote crystallization.

Isothermal crystallization measurements

The temperature and time required for crystallization is an important factor when considering the processing conditions for molding into products. Figure 3 shows a comparison of the crystallization peaks when the molten sample was cooled at 10 °C/min. It can be seen that the higher the recycled PET content in the sample, the higher the temperature at which crystallization begins. It is thought that the impurities in the mixture become the nucleus of the crystal, thereby accelerating crystallization. Figure 4 shows the results of isothermal crystallization measurement based on this result. The horizontal axis is time, and the time when the temperature reaches 220 °C after cooling from 280 °C is defined as 0 min. An exothermic peak due to crystallization was observed immediately after the start of the isotherm at 220 °C. The elapsed time to the top of the peak was 3.53 min for 90 % recycled PET, 8.54 min for 60 % and 17.10 min for 0 %. It can be seen

that the higher the recycled PET content, the shorter the time required for crystallization. It is generally thought that when comparing crystallization at a constant temperature, the higher the melting temperature is, the shorter the crystallization time is. However, the measurement results in Figure 4 show that the crystallization of the recycled PET content of 0 %, which has the highest melting temperature, takes the longest time. This is thought to be due to the fact that a small number of impurities mixed in during the recycling process became the nucleus for crystal formation, which accelerated the crystallization of samples containing recycled PET.

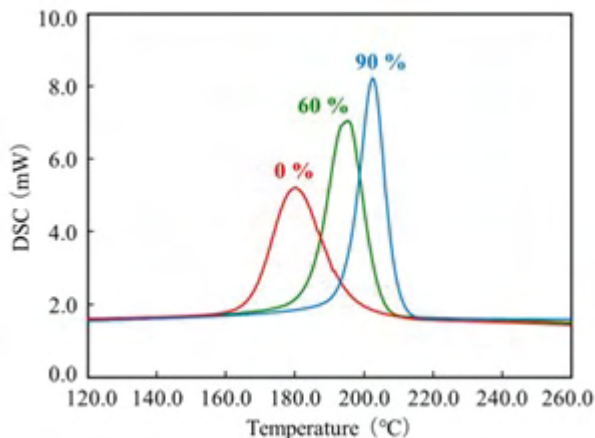


Figure 3: DSC curves of crystallization by constant rate cooling,
Cooling rate : 10 °C/min

Application Showcase

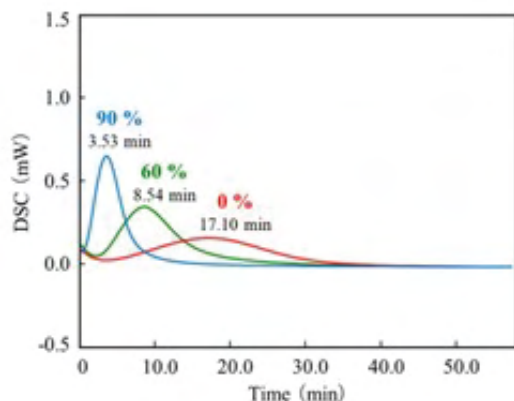


Figure 4: DSC curves of crystallization by isothermal measurement, Isothermal temperature : 220 °C

Sample observation TG measurements

The heat resistance of plastic materials can be evaluated from the starting temperature of mass change by thermo- gravimetry (TG). In addition, changes in the shape and color of the sample can be simultaneously observed by sample observation thermal analysis. Figure 5 shows the results of TG measurement of the samples. In the TG curve, mass loss due to oxidative decomposition of PET is observed from around 300 °C for all samples. For the samples with 60 and 90 % recycled PET content, the mass loss started slowly around 250 °C, showing that the decomposition started at a lower temperature than 0 %.

In the sample observation images at 280 °C, when the melting was completely finished, the 60 and 90 % recycled PET content showed a discoloration from transparent to brown, which is considered to be caused by decomposition, compared to the images at 220 and 250 °C. In order to quantitatively evaluate this color change, L*a*b* color space analysis^{4,5)} was performed on the observed image and the b* values are shown in Figure 5.

As the shape of the sample changed, the b* value also changed at 250 to 270 °C for 0 % recycled PET content and around 240 °C for 90 %. For subsequent changes, the b* value increases from 271.0 °C for 90 %, 273.5 °C for 60 %, and 308.1 °C for 0 %. This is thought to be due to the fact that the higher the recycled PET content, the

lower the molecular weight of the components, and the lower the temperature from which they start decomposing.

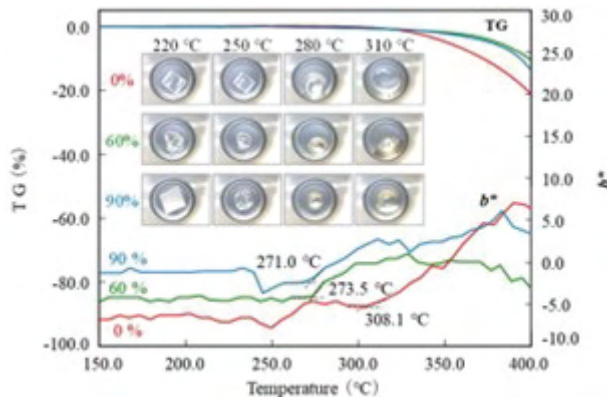


Figure 5: TG and b* curves of PET by Sample observation measurements Heating rate : 10 °C/min

Conclusion

This report compares the differences in thermal properties of three types of PET molded products with different recycled material content which are analyzed using DSC and sample observation TG measurements. As the recycled material content increased, it was observed that the glass transition temperature and melting temperature decreased, crystallization accelerated, and oxidative decomposition and discoloration temperatures decreased. These results suggest that differences in thermal properties are affected by decreases in molecular weight, changes in molecular weight distribution, and contamination and residual impurities from recycling.

The recycling of plastics is being actively pursued worldwide, but the properties of polymer materials may change due to recycling. Thermal analysis is an effective analysis method to examine molding process conditions and to evaluate heat resistance and thermal stability required for products.

Application Showcase

References

1. K. Hirano, N. Iwasaki, Y. Kakuta, M. Sugano, Journal of Material Cycles and Waste Management, 21(5), 165-169 (2010)

2. E. Shimoda, Y. Kasai, N. Okubo, 56th Japanese Conference on Calorimetry and Thermal Analysis, Ooo4 (2020)

3. E. Shimoda, Y. Kasai, N. Okubo, Netsu Sokutei, 48, No.2, 89-90 (2021)

4. S. Ito, E. Shimoda, H. Takahashi, N. Okubo, 5th Central and Eastern European Conference for Thermal Analysis and Calorimetry, OP4.10 (2019)

5. S. Ito, E. Shimoda, H. Takahashi, N. Okubo, Netsu Sokutei, 47, No.2, 78-79(2020)

Differential Scanning Calorimeter (DSC) NEXTA® DSC series



Simultaneous Thermogravimetric Analyzer NEXTA® STA Series

LIPEX[®] FLOW THERMOBARREL EXTRUDERS

Industry-leading bench-top extruders for R&D and cGMP manufacturing of liposomal formulations in both academia and industry.

Innovatively designed to produce a homogenous population of large unilamellar vesicles from a non-homogenous population of multi-lamellar vesicles.

- > High-Throughput
- > Wide Operating Range
- > Fast processing Time
- > Minimizes Process Risk
- > 6X Increase in EFA*
- > 3X Increase in MAOP**



*EFA = Effective Filtration Area

**MAOP = Maximum Allowable Operating Pressure



In Situ FT-IR Spectroelectrochemistry: Experimental Set-up for the Investigations of Solutes and Electrode Surfaces

In situ electrochemical study using a Bruker VERTEX 80 FT-IR Spectrometer, coupled with an A530/P accessory and a Gamry 600 potentiostat

In situ FT-IR Spectroelectrochemistry is a powerful technique for investigating electrochemical reactions at a molecular level. This application describes an experimental setup for in situ FT-IR Spectroelectrochemical investigation of both solutes and electrode surfaces using a Bruker VERTEX 80 FT-IR Spectrometer, coupled with an A530/P accessory and a Gamry 600 potentiostat. This allows for synchronised electrochemical control and spectral acquisition. An exemplary Fe II/Fe III redox couple has been taken for this study.

The described setup offers a reliable and efficient method for in situ monitoring of electrochemical processes, providing valuable insights into molecular changes and reaction mechanisms.

Keywords or phrases: Electrochemical, FT-IR, Spectroscopy, internal reflection, ATR, Bruker, OPUS Software.

Introduction

Electrochemical investigations are a very current topic in research. In recent times, advancements in technology and industry have resulted in a world-wide increase of energy consumption. A future requirement to face this trend is the development of high capacity and as well low weight rechargeable batteries for energy storage. Therefore, studies of electrolyte systems or electrode surfaces are of great importance for possible further improvements.

Also in other fields, like biochemistry or catalysis, electrochemistry is of great benefit to get access to information of molecules, depending on an applied electrochemical potential. For example, of the redox-active centre in biomolecules¹, the reaction behaviour of catalysts or the formation of carbon oxides during alcohol oxidation.

Application Showcase

The combination of FT-IR spectroscopy with electrochemistry offers insight in the molecular change and the reaction process of the studied molecules in addition to the electrochemical response of the experiment. This valuable method can be applied for investigations of electrolytes or of electrode surfaces. With the BRUKER A530/x reflection unit prepared for electrochemical cells the opportunity is given to study both². For an external IR reflection-absorbance spectroscopy (IRRAS) set-up a thin layer configuration is used which allows the study of the electrolyte and the electrode surface.

Alternatively, an internal reflection ATR set-up can be used to analyse the electrode surface directly with limited influence of the electrolyte (Figure 1). Furthermore, for the IR Spectro electrochemical investigation of dissolved molecules in solution Optically Transparent Thin Layer Electrochemical Cells (OTTLE) are also well known for transmission measurements³. Therein the working electrode consist of a semi-transparent metal minigrid. Therefore, the molecules can be studied directly in the vicinity of the electrode surface with transmission measurements.

In this application example we will study the oxidation of ferrocyanide $[\text{Fe}(\text{CN})_6]^{4-}$ and the dependence of the CN⁻ ligand stretching vibration on the oxidation state of the iron centre (Fe II or Fe III). This system is also discussed in detail in the literature⁴. Additionally, we determine the layer thickness within the external reflection mode.

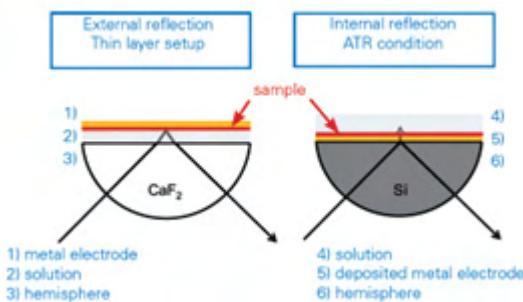


Figure 1: Different measurement modes of the A530/x reflection unit. On the left-side external reflection (materials: CaF₂, BaF₂), on the right-side internal reflection (materials: Ge, Si).

Instrumentation

The experiments were conducted with a purged VERTEX 80 FT-IR spectrometer equipped with the A530/P accessory and a mid-band MCT detector. A representation of the reflection cell A530/P as used in the experiment is depicted in Figure 2, showing the installation of the different components, a glass body and electrodes. The measurement parameters were 4 cm⁻¹ resolution and 100 scans.

A MIR polarizer was installed, and p-polarized light was used for the investigations. The experiments were controlled by the Gamry 600 reference potentiostat using trigger functionality with the FT-IR spectrometer. A thin gold plate disk was used as working electrode, and silver and platin wires as quasi-reference and counter electrodes.

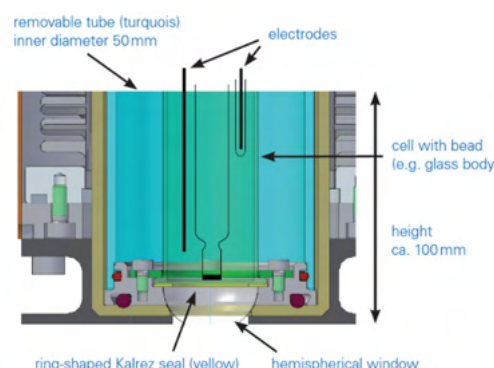


Figure 2: Design of the reflection cell A530/x with installed glass tube.

Investigations were performed on a 20 mmol/l solution of potassium ferrocyanide $\text{K}_4[\text{Fe}(\text{CN})_6]$ in water and additional 1 mol/l potassium chloride KCl as supporting electrolyte. For the study of the dissolved metal complex the solution was measured using a silicon hemispherical window (F530-8) in the ATR mode with the working electrode placed 1 mm above the window.

Investigation in the external specular reflection mode were performed using a barium fluoride hemispherical window (F530-17) and a gold electrode pressed against

Application Showcase

the window creating a thin layer between them.

Results and Discussion

A cyclic voltammogram (current at the working electrode plotted versus the working electrode potential), depicted in Figure 3 of this redox system was recorded to get an overview of the oxidation and reduction potentials. Later, the solution of potassium ferrocyanide was investigated with in situ FT-IR Spectro electrochemistry.

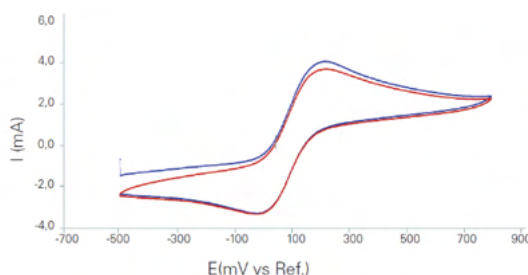


Figure 3: First and second run of a cyclic voltammogram with 0.1 V/s of ferrocyanide $[\text{Fe}(\text{CN})_6]^{4-}$ in 1 M KCl solution.

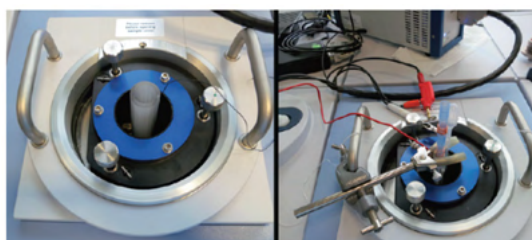


Figure 4: Pictures of the experimental setup. Reflection unit with polymeric flask installed (left), complete cell installed and connected (right).

The quasi-reversible redox process for the reaction $[\text{Fe}(\text{CN})_6]^4 \rightleftharpoons [\text{Fe}(\text{CN})_6]^{3-} + \text{e}^-$ can be seen in this system and the oxidation and reduction peaks were well resolved. The in situ FT-IR Spectroelectrochemical experimental setting is depicted in Figure 4.

The experiment can be controlled in a way that the potential is set in steps to a desired value. Between every potential increase the value can return to a specified reference potential to control the reversibility of the electrochemical process. A diagram of one experimental run is shown in Figure 5 exemplarily, starting from

$E_{\text{start}} = -0.3 \text{ V}$ to $E_{\text{end}} = 0.8 \text{ V}$ and returning after every step to a reference potential $E_{\text{ref}} = 0 \text{ V}$.

After a certain delay, which is also specified in the control script, at every level shown in the graph, a defined number of IR spectra are co-added and averaged.

After the start the experiment runs independently with a duration of approximately twenty minutes in this example. The collection of IR spectra can be analysed and presented in different ways.

One common possibility is the use of SNIFT-IRS type diagrams (Subtractively, Normalized Interfacial Fourier Transform IR Spectroscopy)⁵, in which the y-scale of the graph represents the following $\Delta R/R = (R_x - R_0)/R_0$. An example of it is shown in Figure 6 for the oxidation of $[\text{Fe}(\text{CN})_6]^{4-}$ in the spectral range between 2200 and 1950 cm^{-1} and with cell potentials ranging from -0.3 V to 0.8 V. As can be seen clearly the decrease of the reduced form of the molecule $[\text{Fe}(\text{CN})_6]^{4-}$ in solution is indicated in this representation by the increasing band at 2039 wavenumbers. The formation of the oxidized form ferricyanide $[\text{Fe}(\text{CN})_6]^{3-}$ in solution can be seen by the decreasing band at 2115 cm^{-1} . Additionally, a slightly yellow colour of the solution could be observed.

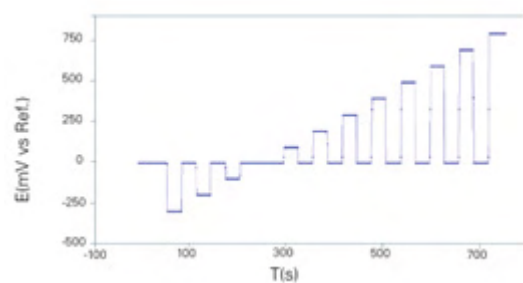


Figure 5: Potential change during an experimental run. Depicted like given in chronoamperometry. IR spectra are measured at the defined potential levels.

When the potential returns to a value of -0.3 V the spectrum resembles again the spectrum of the starting potential, which points out the reproducibility of the experiment. So again, the reduced form $[\text{Fe}(\text{CN})_6]^{4-}$ is present in solution.

Application Showcase

Alternatively, the course of the reaction can be observed with rapid scan functionality showing directly the change in absorbance of the infrared bands during the measurement in an OPUS 3D-plot. Therefore, the Time-Resolved-Spectroscopy (TRS) postrun window of the OPUS software offers useful functionality. A plot for the oxidation of the ferrocyanide solution measured in ATR conditions is shown in Figure 7.

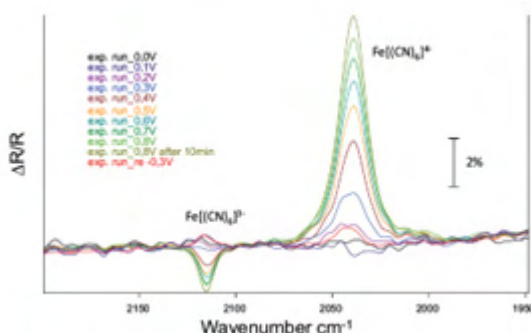


Figure 6: IR spectra of the ferrocyanide solution measured at potentials ranging from -0.3 V to 0.8 V shown as SNIFTIRS type spectra.

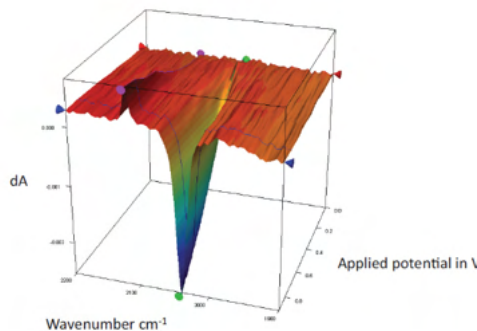


Figure 7: Three-dimensional representation of the oxidation of a ferrocyanide solution at potentials ranging from -0.3 V to 0.8 V, shown as 3D-plot as offered in the OPUS software.

For the study of small layers on electrode surfaces and electrolytes, alternatively to the ATR mode, a thin layer experimental set-up can be used. For this external reflection mode of the electrochemistry accessory one of the important parameters to know is the thickness of the layer, created between the electrode surface and the hemispherical window.

The thickness can be determined easily after the positioning of the metal working electrode on top of the hemispherical window (low refractive material) and prior to the addition of the electrolyte.

For the determination the interferences are used which arise from the IR beam path going through the flat surface of the hemispherical window of the cell. Figure 7 shows the interference pattern without electrolyte in the cell which calculates a layer thickness of 27 μ m.

The path length can be determined easily with the Layer Thickness function as integrated in the OPUS software. By doubling this value for the IR path (in and out of the electrochemical cell), the IR beam would penetrate about 50 μ m of the electrolyte solution during the measurement.

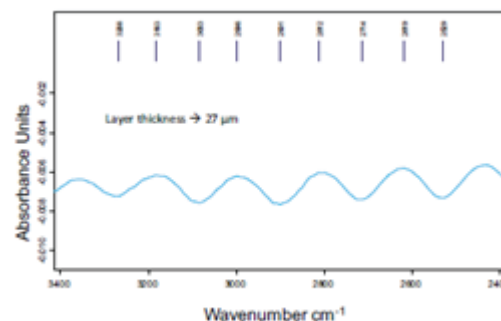


Figure 8: IR spectra of the empty electrochemical cell measured in the external reflection mode using a barium fluoride hemispherical window. The layer thickness in this measurement between electrode surface and window is determined to 27 μ m.

Conclusion

The electrochemical oxidation of a metallic complex, ferrocyanide $[\text{Fe}(\text{CN})_6]^{4-}$ was studied with FT-IR Spectroelectrochemistry.

This combined analysis method offers the possibility to investigate the molecular change of this compound depending on the applied electrochemical potential. The oxidation to ferricyanide $[\text{Fe}(\text{CN})_6]^{3-}$ was illustrated in the form of a SNIFT-IRS spectrum and a 3D-plot with the OPUS software. One main advantage of the set-up reported here is, that the potentiostat and the spectrometer are connected by a trigger functionality for an all-over communication.

After setting the experimental parameters and the desired potential procedure, the measurement can be simply started in OPUS and will run automatically.

Application Showcase

The resulting spectra will be well sorted and assigned to their corresponding potential for subsequent evaluation.

In the end, the technical realization of the combination of FT-IR spectroscopy and electrochemical investigations makes the *in situ* monitoring of electrochemical processes easy and reliable.

References

1. C. Berthomieu, L. Marboutin, F. Dupeyrat, P. Bouyer, *Biopolymers* 2006, 82 (4), 363–367.
2. Bruker Product Note M140 - 08/12: A530/P or A530/V Reflection Unit prepared for Electrochemical Cell.
3. S. R. Domingos, H. Luyten ,F. van Anrooij, H. J. Sanders, B. H. Bakker, W. J. Buma, F. Hartl, S. Woutersen, *Rev. Sci. Instrum.* 2013, 84, 033103.
4. S. M. Rosendahl, F. Borondics, T. E. May, T. M. Pedersen and I. J. Burgess *Anal. Chem.* 2011, 83 (10), 3632–3639.
5. Kabbabi, R. Faure, R. Durand, B. Beden, F. Hahn, J.-M. Leger, C. Lamy, *J. Electroanal. Chem.* 1998, 444, 1–53.



FT-IR Spectrometer VERTEX 80/80v



INVENIO®

Flexible FT-IR Spectrometer

Exactly As You Need It



Features:

- ◆ Spectral range expansion from FIR to UV/VIS
- ◆ Up to 7 software-controlled detectors
- ◆ Spectral resolution down to $< 0.085 \text{ cm}^{-1}$
- ◆ Time resolved spectroscopy down to the nanosecond timescale
- ◆ Second sample compartment for two parallel set ups
- ◆ Simultaneous FIR/MIR measurements
- ◆ Accepts any sampling accessory with quick swappable mount
- ◆ Intuitive software with guided workflows



Seeing beyond

Metallic Grain Structures and Their Microscopic Analysis

Understanding Metallic Structures with Zeiss Microscopy Solutions

Metallic materials are interpreted in terms of their inner structure – known as the grain structure – in addition to a wide range of other chemical and physical properties. This inner structure is referred to as the “macrostructure” or “microstructure” depending on the size of the elements being observed. The grain structure is typically adapted to the technical application of the material and can be viewed with conventional light microscopes, provided that the specimen being examined has been appropriately prepared. This preparation process is also referred to as “metallographic preparation.” Depending on the composition of the metal, its processing history (e.g. heat treatments and forming processes) and the expected structural properties (e.g. grain size, content of non-metallic inclusions), this metallographic preparation involves selecting the mechanical or electrolytic processing procedure as well as the subsequent chemical and microscopic contrasting and enlargement.

This text is intended to provide a practical and readily comprehensible insight into this topic.

Keywords or phrases: Grain structure, microscopy, etching, microstructure, Zeiss

What is a grain structure and why should it be examined with a microscope?

A metallic grain structure consists of individual, typically microscopic crystalline areas known as “grains.” Macroscopic grains are less common and, depending on the base metal, are more frequently found in nonferrous materials (e.g., aluminium, copper, zinc). Grain structures with details that can be seen with the

Application Showcase

naked eye, or a magnifying glass are referred to as macrostructures.

If, on the other hand, a microscope (stereo, reflected light or digital) is required to assess the material, the term microstructures is used.

These grains form from the molten material when it solidifies, interact with one another and with “foreign elements” (phases, contamination), and of course also react to subsequent external influences – such as chemical processes (corrosion), chemical and/or physical influences (e.g. heat treatment processes) or purely mechanical influences, such as downstream forming processes.

The structure, size and orientation of the grains result from the material composition (alloy) used and the way the material is made (forging, casting, or additive manufacturing).

Once metallographic preparation is complete, visible light can interact with the prepared structural grains and their crystal shapes and boundaries under a light microscope, making them visible. This typically occurs at magnifications of 25x to 1000x, which corresponds to the limits of traditional light microscopy.

Lattice defects, structures and elements at the sub-microscopic level (<1 µm) and down to the atomic level are assessed using electron microscopes rather than light microscopes. As such, electron microscopes (SEM, TEM) that can be extended by means of optional element analysis equipment (EDX: e.g., ZEISS EVO 10/15/25; WDX) are used if greater magnifications are required.

Based on the microscopic image, it is then possible to draw conclusions regarding the characteristics of the material or the workpiece (materials that are part of an overall system). For example, the grain size and general microstructure can be used to determine the degree of hardness and resilience; certain phases may cause the material to become brittle or influence its resistance to

microstructure are not only a means of evaluating characteristics for the design and processing stages but also play a significant role in assessing cases where damage has occurred.

Structural elements that can be evaluated using a light microscope include (Figure 1):

- Grains/crystallites and their grain boundaries
- Intermetallic phases and precipitates
- Nonmetallic inclusions (NMI) and phases

The evaluation is based on the following criteria:

- Type and form
- Size and number
- Distribution and orientation

Based on all of this information, it is then possible to create a comprehensive description of the microstructure (of the grain structure) and draw conclusions regarding its potential characteristics.

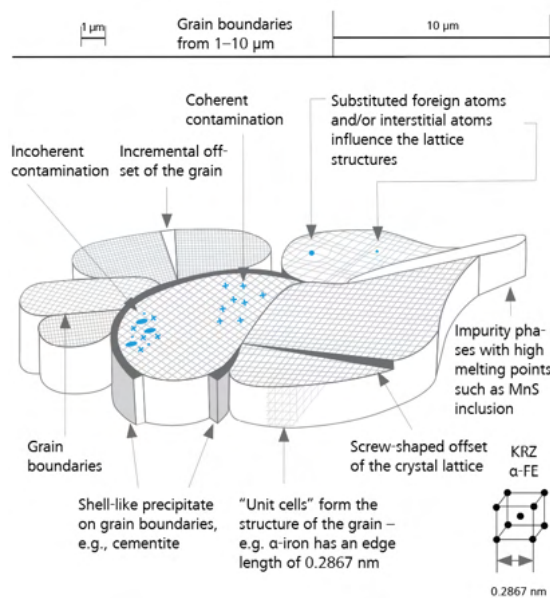


Figure 1: Schematic grain structure of a ferrous material

The materials used in practical applications today are a mixture of various chemical elements sometimes also referred to as “alloys.” Steel and cast iron are essentially alloys based on iron (Fe) with carbon (C) alloying additions, which are responsible for the hardness of the

Application Showcase

ferrous material. The carbon may take the form of a pure element (lamellar and globular graphite in cast iron, Figures. 2 and 3) or may be present as an intermetallic phase, which is also referred to as iron carbide Fe_3C or cementite.

In the case of soft, low-carbon ferritic steels, the hard cementite is typically precipitated along the boundaries of the ferritic grain in the form of tertiary cementite or as a small proportion of pearlite (Figure 4). Iron carbide Fe_3C occurs as a lamella in the harder structural element pearlite and this lamellar structure is made visible following etching. This banding, along with lower reflection of light, make the pearlite appear darker than the ferrite (Figures 2 and 5).



Figure 2: Pearlitic cast iron with lamellar graphite, etched with nital. The carbon is primarily present as graphite in a lamellar form, which results in reduced strength. The pearlitic matrix itself exhibits a sufficiently high degree of hardness.

Image taken with ZEISS Axio Imager, 50x objective, brightfield

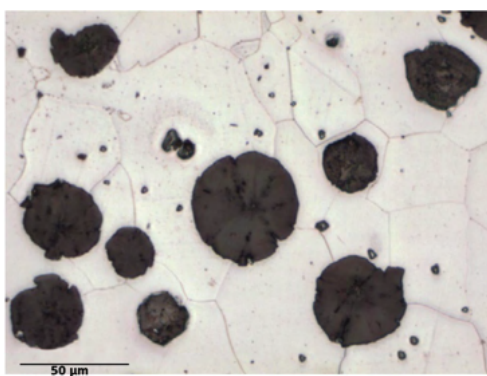


Fig. 3: Ferritic cast iron with spheroidal graphite, etched with nital. The carbon is primarily present as graphite in a spherical form. The spherical form results in improved strength in comparison to lamellar cast iron, but the hardness of the material is lower due to the lack of cementite in the purely ferritic matrix.

Image taken with ZEISS Smartzoom 5, at approx. 500x magnification

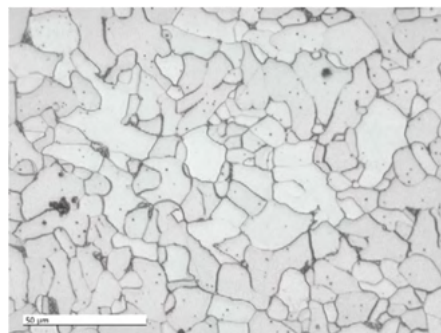


Fig. 4: Ferritic steel with approx. 0.1 % C, etched with nital. The carbon is primarily present in the form of cementite and as a low proportion of pearlite between the ferritic grains. The matrix, which is therefore nearly purely ferritic, has a low degree of hardness but very good resilience.

Image taken with ZEISS Smartzoom 5 at approx. 500x magnification, coaxial illumination with low proportion of ring light



Fig. 5: Ferritic-pearlitic steel with approx. 0.2 % C, etched with nital. The carbon is primarily present as a cementite lamella in a harder proportion of pearlite adjacent to the ferritic grains. This causes the cementite to appear streaky. The pearlitic grain reflects less light than the ferritic grain and thus appears darker. A matrix of this type has a higher degree of hardness than the steel in image 4, but a lower resilience.

Image taken with ZEISS AxioLab, 50x objective, brightfield

Other alloying elements may include metals such as aluminium (Al), chromium (Cr), manganese (Mn), vanadium (V), nickel (Ni), molybdenum (Mo) and silicon (Si), which through their inclusion cause the iron lattice to have certain properties.

Other nonmetal elements such as nitrogen (N), hydrogen (H), oxygen (O), phosphorus (P) and sulphur (S) are frequently undesirable “steel parasites,” as they typically negatively impact the properties of the metal. Their products (e.g. oxide and sulphide) are often analysed in the course of determining the NMI (determination of non-metallic inclusions, also frequently referred to as determination of steel purity). However, within certain limits they can also serve as desirable alloying elements.

Application Showcase

How is this matrix made visible?

Metallographic preparation tailored to the material forms the basis for the correct depiction of the grain structure.

A wide range of preparation methods can be used depending on the material composition and the question being addressed. There is sufficient literature available regarding metallographic preparations. Furthermore, manufacturers of metallographic preparation equipment and consumables provide procedural documentation on their websites, which can be viewed and downloaded as a guide when getting started.

www.struers.com

Metallography is a type of destructive physical testing. The component undergoing metallographic testing is destroyed in nearly all cases (as in the production of metallographic specimens) or at least slightly damaged. However, it may still be possible to use the component in some cases – such as in the case of on-site component testing. The following section briefly describes the steps involved in producing a specimen for metallographic examination.

The first step is taking the sample. To this end, a wet abrasive cutting process is used to take a representative sample from the workpiece being examined. A thin, rapidly rotating disc containing an abrasive is used for this purpose (Figure 6).

This sample is intended to represent the structural condition of the entire component or a specified area of its structure (welding seam, joints, heat-treated areas). This naturally means that the cutting process should be designed to treat the sample with care, so that it is not subjected to any damage that modifies its structure. This is achieved through the structural design of the cutting discs and equipment, which are tailored to the material and application scenario in question.

The cutting process establishes the surface that will be subsequently examined under the microscope.

Next, an embedding process is used to fix the cut pieces so they can be handled more easily and to standardize their dimensions (Figure 7). Epoxy or acrylic resin is typically used to fix the pieces; cold (up to approx. 100 °C, at atmospheric pressure or in a vacuum) or warm (at max. 350 bar and 180 °C) embedding press machines can be selected for this step.



Fig. 6: Wet abrasive cutting machine with clamped gear wheel for taking a sample of a section of a gear tooth. This section, which is typically induction- or case-hardened, will be examined with respect to its structure and hardness and thus needs to be separated from the component.



Figure 7: Variety of embedded samples of varying shapes. Performing embedding with various synthetic resins ensures a good preparation process outcome and makes this procedure efficient.

While the prerequisites for an ideal preparation and therefore a good representation of the structure are established during the cutting and embedding steps, the grinding and polishing process is likely the most important step in terms of the microscope examination. During this process, the macroscopic roughness of the cut surface is reduced to the point of attaining a reflective surface. If the intention is only to make the macrostructure visible, a few coarser grinding steps and

Application Showcase

contrasting with acidic or alkaline solutions are sufficient. A reflective surface is not required for this, as the specimen will typically be examined using a stereo microscope (Figure 8).

Nonetheless, the mirror finish is required to make the microscopic elements of the structure visible under a reflected light microscope. It is achieved by gently milling the surface with fine to very fine abrasives following surface grinding.

Milling continues until nearly all damaged areas are removed from the surface, typically using diamond, aluminium oxide or colloidal silicon dioxide on appropriate polishing cloths and discs. The success of the preparation can typically be checked early on using the differential interference contrast (DIC), which shows even the slightest deformations in the surface (Figure 9). If DIC is not available, observing the specimen under brightfield conditions is sufficient in most cases.

The sample should only be etched after this step. The etching process enhances contrasts that are invisible or only visible to a limited extent under brightfield conditions and allows the microstructure to be examined with a high degree of accuracy. Typically, only weak acids are used for this step.

Weak nitric acids with an alcohol content of 1–3 % (nital are very often used for unalloyed and low-alloyed carbon steel (cf. Figures 2–5). Corrosion-resistant steel requires special etching processes, such as colour etching, which influences the interference of the microscope's light on the surface, or electrolytic etching (Figures 10 and 11).



Fig. 8: Welding seam ground on two levels of SiC film, followed by macro etching with 5 % aqueous nitric acid.

Image taken with *ZEISS Stemi 508 stereo microscope at 15x magnification*



Fig. 9: Ferritic steel with titanium carbide and oxide inclusions following mechanical preparation to 1 μm diamond. Fine traces of deformations can still be observed in the differential interference contrast image. The sample has not been etched.

Image taken with *ZEISS Axio Imager, DIC, 100x objective*

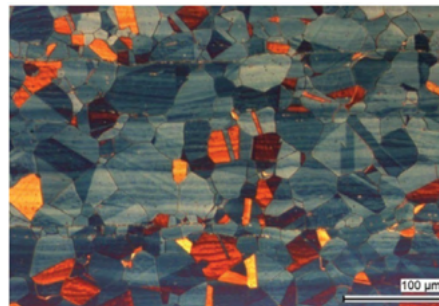


Fig. 10: Corrosion-resistant austenitic steel after final polishing with OP-S and subsequent Lichtenegger and Bloech color etching. Austenite grains with twins and ghost lines in the direction of deformation become visible.

Image taken with *ZEISS Axio Imager, brightfield, 20x objective*



Fig. 11: Corrosion-resistant austenitic-ferritic steel (duplex) following electrolytic etching in 20 % sodium hydroxide solution. The austenite grains (light brown) are embedded in the bluish-brown ferritic matrix.

Image taken with *ZEISS AxioLab, DIC, 20x objective*

The desired structures only become visible when there is an ideally coordinated interplay between the preparation technique, the appropriate chemical or

Application Showcase

electrochemical etching process and the microscopic contrasting technique (brightfield, DIC, polarization) as well as the desired resolution (of the smallest discernible feature).

Which contrasting techniques can we now use to characterize the structural properties of metals?

The option of using different contrasts on a light microscope enhances the analysis of metallic structures. This type of contrasting, which can take place either on its own or in conjunction with preceding chemical or electrolytic contrasting procedures, is also referred to as “optical etching.” The following section discusses the most common contrasting techniques used for routine analysis of structures and provides examples of several typical applications.

Technique	Application	Measuring	Documentation
Reflected light brightfield (Fig. 12)	Standard (e.g., grain boundaries, nonmetallic inclusions, phases, fissures, oxidation)	●	●
Reflected light darkfield (Fig. 13)	Lacquer and plastic coatings, composite materials, glasses, corrosion products	●	●
Reflected light DIC (Fig. 15)	Deformation, protrusions	●	●
Reflected light polarization contrast (Figs. 16 and 17)	Grain size, grain shape and grain orientation following electrolytic etching (Barker) for Al and Al alloys; grain structure in unetched condition with hexagonal lattice types (e.g., Co, Ti, Mg, Zn, Zr)	●	●
Reflected light fluorescence (Figs. 18 and 19)	Fissures, pores (when open during embedding)	●	●

Table 1: Examples of applying contrasting techniques for examining metallic structures

The **brightfield** is a standard technique for all types of material analyses. Fissures and pores, nonmetal phases and oxidation products are first observed in an unetched condition, as they typically exhibit different reflective behaviour than the base metal material. The location of fissures and pores in relation to other structural characteristics, on the other hand, can typically only be evaluated if appropriate chemical etching has been carried out (Figure 12).

The **darkfield technique** is used less frequently in metallurgical microscopy than it is in the microscopy of nonmetal materials. However, this contrasting technique also offers several advantages for metals, as well as when evaluating coloured structures such as layers of lacquer or plastic coatings on metal substrates. This contrast can also be used to evaluate corrosion products (Figure 13). Darkfield microscopy can be used to show very fine scratches on polished samples as a method of examining the grinding quality.



Fig. 12: Laser welding seam on high-alloy steels with fissures and pores following electrolytic etching. These are also visible in the unetched condition, but the intercrystalline course of the fissures can only be evaluated after etching has been completed.

Image taken with *ZEISS Axio Imager, brightfield, 5x objective*

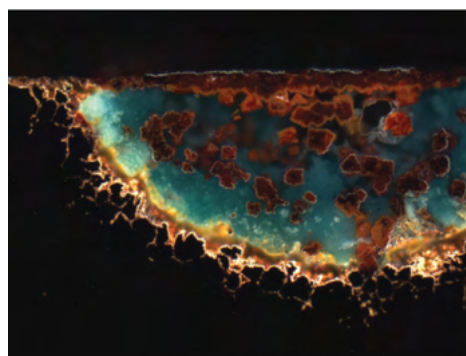


Fig. 13: Corroded area on a brass pipe, unetched. Reflective areas appear dark (metal substrate) under the darkfield microscope, while the corrosion products can be observed in their own color.

Image taken with *ZEISS Axio Imager, darkfield, 20x objective*

The **differential interference** contrast is a useful tool for analysing very fine deformations that may still be present in the surface after polishing (cf. Figure 9). Checking the quality of polishing prior to the etching process can prevent additional effort being required

Application Showcase

during preparation. DIC can also be used to distinguish hard and soft structural elements, as hard phases are removed to a lesser extent than softer ones during the final polishing process. They therefore “protrude” from the surface (Figures. 14 and 15).

This minimal difference is not typically visible under a brightfield microscope but can be seen in DIC. As such, this contrast can be used to make a qualitative distinction between the hardness of different phases. A further key advantage is the possibility of making grain structures such as grain boundaries visible even in an unetched condition (Figure 15). The structure can therefore be evaluated prior to etching, so chemicals that pose a risk to health do not need to be used on materials that are difficult to etch (corrosion resistant materials). However, a perfect final polish is required in this case.

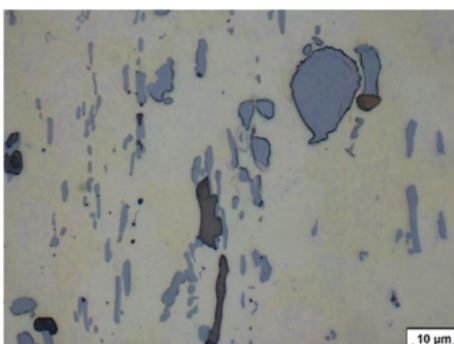


Fig. 14: Copper alloy after final polishing. Due to their reflectivity, the various phases appear to have different colors under a brightfield microscope.

Image taken with *ZEISS Axiolab, brightfield, 100x objective*



Fig. 15: Copper alloy like that in Fig. 14. Due to their ablation behavior, the phases of varying hardnesses have varying heights, which are only visible in DIC microscopy. This enables a qualitative distinction between their hardnesses. At the same time, the grain structure can already be made visible in the unetched condition.

Image taken with *ZEISS Axiolab, DIC, 100x objective*

The **polarization contrast** is primarily used in the analysis of materials with a hexagonal lattice structure. This includes titanium, zinc and magnesium in particular, as well as a range of other materials (Fig. 16). However, aluminium and its alloys can also be analysed under polarized light after being etched appropriately.

This requires electrolytic etching with tetrafluoroboric acid, which is known as Barker etching (Figure 17).

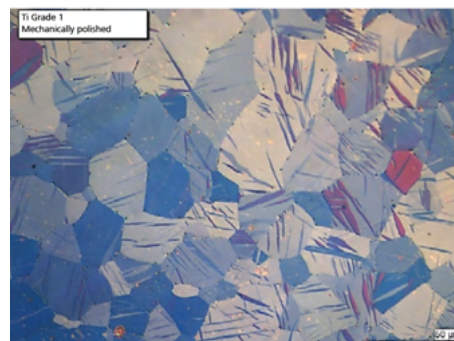


Fig. 16: Technically pure titanium (Grade 1) following mechanical polishing, seen under a polarization contrast microscope. Unetched surface. The polarized light is enhanced or eliminated on the crystal faces due to the hexagonal lattice structure, which manifests itself as a contrast between light and dark. The image appears in color due to a so-called $\lambda/4$ plate.

Image taken with *ZEISS Axio Imager, polarization contrast, 20x objective*

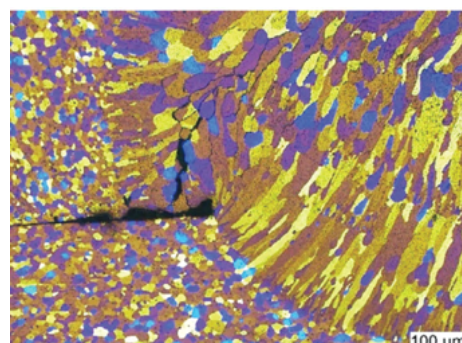


Fig. 17: Aluminum welding seam following electrolytic etching with tetrafluoroboric acid (Barker etching), seen under a polarization contrast microscope. The etching creates a layer of oxide of varying thickness depending on the orientation of the crystals; the polarized light can interfere in this oxide layer. This also results in elimination and enhancement effects.

Image taken with *ZEISS Axio Imager, polarization contrast, 5x objective*

is a further contrasting technique that can be used in metal and material microscopy. This method exploits the fact that certain materials that are excited at a certain wavelength emit visible light at another wavelength. These fluorescent powders (e.g., Epodye)

Application Showcase

are mixed with the embedding agent (typically transparent epoxy resin) during the embedding process and, together with it, penetrate existing and open pores and fissures. This procedure is supported by vacuum impregnation. Following curing and preparation, the microscope's light in the blue spectrum excites the fluorescent dye, which then emits light in the yellow-green spectrum. The filled pores or fissures are illuminated in yellow green (Figures 18 and 19).

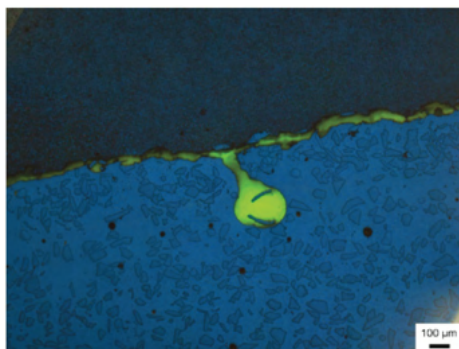


Fig. 18: Pore and fissure between a WSC coating and the steel to which it is applied. This is illuminated in yellow-green in the corresponding microscope contrast because the fissure was penetrated by embedding agent with fluorescent powder. The fissure was therefore present prior to embedding and may have arisen during fabrication; however, it could theoretically also have occurred during the cutting process and be a preparation artifact.

Image taken with ZEISS Axio Imager, fluorescent contrast, 5x objective

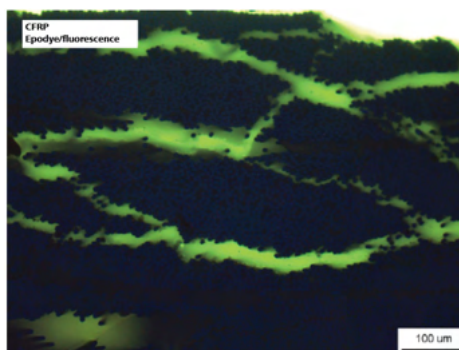


Fig. 19: Fissures in a carbon fiber composite material

Image taken with ZEISS Axio Imager, fluorescent contrast, 20x objective

Conclusion

The light microscope equipment

Reflected-light microscopes are used to visualize structures in the range from mm to approx. 1 μm

(10x/20x/50x/100x objectives are typical for the material microscope. Figure 20). The design can be either upright or inverted, which is advantageous for large specimens or when viewing clamped specimens in specimen holders. High-definition stereo microscopes, on the other hand, are used less frequently for structural interpretations. The image generated by the microscope must be rendered faithfully and be suitable for integration into current documentation systems. Because the illumination and contrasting of the reflective samples is performed by the imaging optics – the microscope objective – special requirements apply to the design and light guide.

Furthermore, the objective must exhibit precise field flattening characteristics for object measurement. These types of objectives, which are specially optimized for reflected light specimens, can be recognized by the abbreviation "EPI" (e.g., the ZEISS 50x EC EPIPLAN # 422070-9961-000). Among other things, special antireflection coatings reduce the reflections from the object and the optical calculation does not provide for a cover glass. The digital camera requirements for metallic samples must be optimized for measuring and documentation purposes. A highly dynamic imaging camera chip displays metal surfaces and their high levels of contrast in an ideal way. Special industrial software packages (such as "ZEN core" and its material modules) are available to provide assistance in using a camera of this type (for example, the ZEISS Axiocam 305) in practical settings. Microscopes for beginners, such as the "ZEISS Primotech," include the most common contrasting techniques and can also be used with simplified "MATSCOPE" software and tablet solutions ("MATSCOPE" for iPads).

The rapid optical development of the "digital microscope" is also making it an increasingly interesting tool for structural analyses. These devices are becoming increasingly significant thanks to their ease of use and their combination of the advantages of stereomicroscopy with those of reflected light microscopy. They therefore also cover a relatively broad magnification and application range. In particular,

Application Showcase

reflected-light microscopes do not offer the same opportunity to digitally post-process images with a wide range of measuring tasks. However, digital microscopes are unable to keep pace with the good resolution offered by reflected-light microscopes, which is a drawback when working with very small structural elements (cf. also Figures 3 and 4).

Special optics must be used, as the excitation and object lighting are directed through the same optical system. These are denoted by the abbreviation "EPI."

Cameras must be capable of processing high contrast values.

References

1. Schumann/Oettel: Metallografie [Metallography]. 14th edition. WILEY-VCH Verlag GmbH & Co. KGaA, Weinheim. ISBN 3-527-30679-X
2. Petzow: Metallographisches, Keramographisches und Plastographisches Ätzen [Metallographic, ceramographic and plastographic etching]. 6th edition. Brüder Borntraeger, Stuttgart 1994. ISBN 3-443-23014-8
3. ZEISS – Lichtmikroskopie, Bibliothek der Technik [ZEISS – Light microscopy, library of technology]. ISBN 978-3-86236-088-8
4. Mikroskopische Betrachtungen zum Eisen Kohlenstoffdiagramm [Microscopic observations of the iron carbon diagram], tbd
5. Domke, 10th edition, "Werkstoffkunde und Werkstoffprüfung" [Materials science and materials testing]
6. Application note: DE_42_013_151_Applications_of_microscopy_in_additive_manufacturing.pdf



Axiovert.A5/7



AxioLab.A5 MAT



Smartzoom 5

Fig. 20: Versions of light microscopes for structural analyses.

Zeiss Microscope for Material Science Research

inkarp®
Your Knowledge... Our Solution...!
Authorised India Partner

Your Versatile Systems for
the **Materials Lab and Smart Documentation**



Seeing beyond

Axiovert 5

- Comprehensive Material Analysis
- Advanced Imaging for Metallography and Material Science
- Non-Metallic Inclusion Analysis



Axio Imager 2

- Precise Particle Analysis
- Correlative Automated Particle Analysis (CAPA)
- Seamless Microscopy Workflow

ZEISS Axiolab 5

- Efficient Metallographic Analysis
- High-Quality Documentation and Inspection
- Precision in Sample Preparation and Mineralogy



analytica Anacon India

23-24-25 April 2025, Mumbai

INDIA LAB EXPO

Booth No: G031

FEBRUARY 2025
info@inkarp.co.in



Fully Automated High-Throughput Battery Development

Example Workflows for Battery Research using the Chemspeed FLEXSHUTTLE

The global demand for advanced energy storage solutions is rapidly increasing driven by the proliferation of electric vehicles, portable electronics and energy storage technologies. Battery research and development plays a huge role in meeting these demands. However, manual battery development processes are time consuming, labour-intensive and prone to inconsistencies. This necessitates the adoption of high-throughput, automated approaches to accelerate and optimise battery research processes.

This application note provides an overview of the Chemspeed's FLEXSHUTTLE platform and its integrated workflow management ARKSUITE software for high-throughput automated battery development processes.

Keywords: Battery, automated, workflows, high-throughput, Chemspeed FLEXSHUTTLE

Introduction

The surge in demand for efficient and sustainable energy storage devices has driven the need for advanced batteries with enhanced performance, longevity and safety. Traditional methods are often slow due to extensive manual experimentation, testing and not to mention, prone to errors.

This article highlights Chemspeed's fully automated solution for battery research. Example workflows on the FLEXSHUTTLE platform shows how each step significantly accelerates battery development lifecycle.

Chemspeed's solution

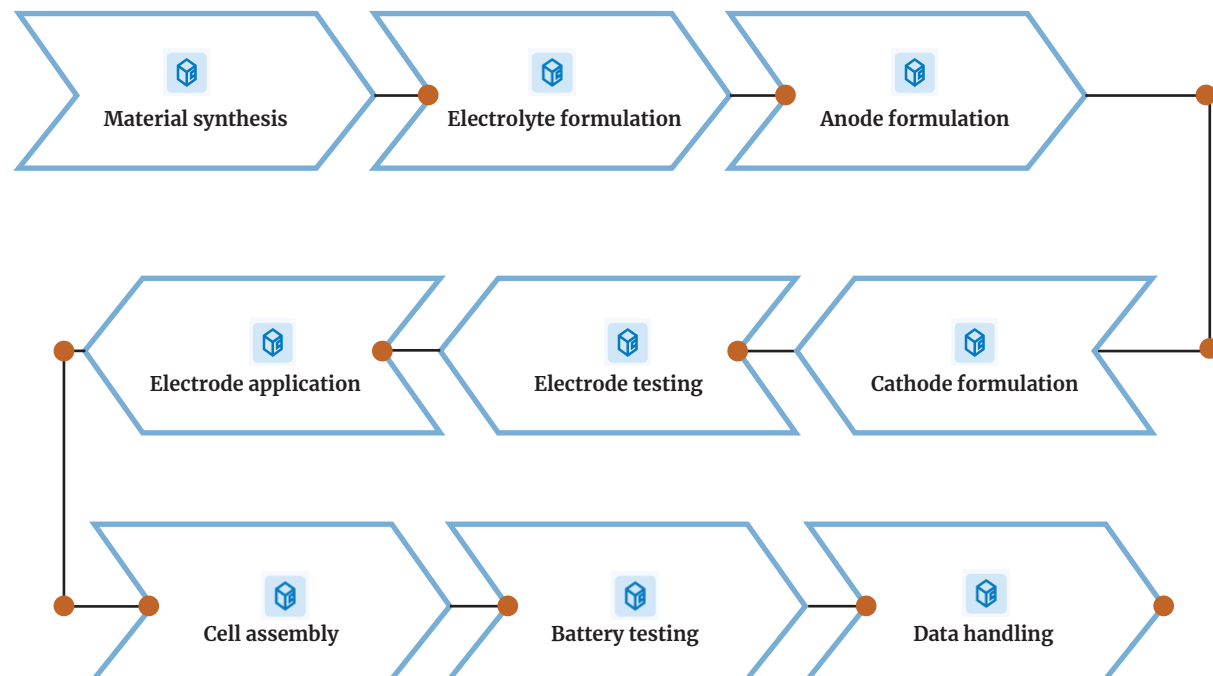
The modular design enables significant efficiency increase combined with high quality and maximum ease of use.

- Design your automated laboratory
- Navigate on the system with shuttles
- Model, execute and control multiple workflows
- Ensure conditioned atmosphere as required by means of tight enclosure
- Dispense gravimetrically liquids, pastes and solids from small to large amounts in high accuracy

- Formulate battery slurries (anode and cathode)
- Measure and adjust rheology
- Apply battery slurry via roll-to-roll coating followed by heat curing and calendering
- Punch electrodes in different formats and assemble them in coin or pouch cells
- Characterize conductivity, rechargeability and other battery properties

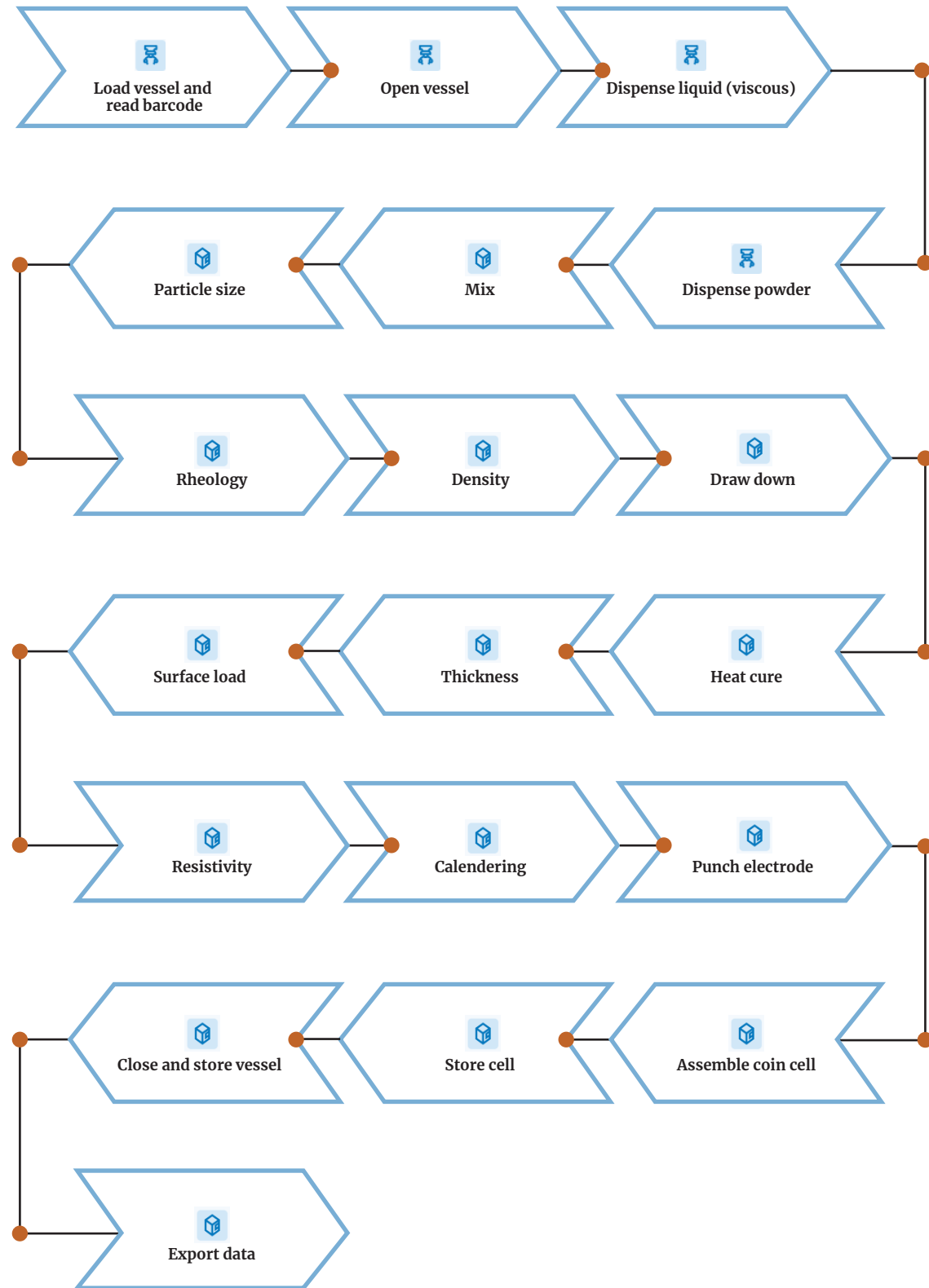
Example Workflows

The workflow below showcases an example workflow indicating generic steps for battery development.



Application Showcase

Example Workflow with detailed steps for coin batteries-



Application Showcase

Action	Tools and Function
Load vessel and read barcode	Multigripper Robotic Tool for Vials/Plates/ISYNTH Drawers - For transfer of vials, centrifuge tubes etc
Open vessel	Screw capping / Decapping Robotic Tool / Screw Capper - For opening, closing and discarding vials and caps
Dispense liquid (viscous)	Overhead gravimetric dispensing unit for highly viscous liquids / GDU-HV - For direct gravimetric dispensing into a target as a formulation vessel
Mix	FLEX MIX (Dual Asymmetric Centrifugation) - Fully integrated mixing system for dispersing / mixing a variety of materials: With a large range of viscosities in any combination - e.g. colloids, fluids, powders, pastes, creams, grease, resins, inks and paints mixtures
Particle size	FLEX PARTICLE SIZE (dynamic light scattering) - Automatic system for particle size measurement
Rheology	FLEX RHEOLOGY - Fully integrated automatic system for rheology measurement of liquid samples
Density	FLEX DENSITY - Automatic system for specific gravity / density measurement of liquid samples
Draw down	FLEX DRAW DOWN & HEAT CURING - Automatic roll-to-roll draw down system for metallic foil, including in-line heat curing
Heat cure	FLEX DRAW DOWN & HEAT CURING - Automatic roll-to-roll draw down system for metallic foil, including in-line heat curing
Thickness	FLEX ELECTRODE CHARACTERIZATION - Fully integrated automatic system for coating characterization: surface loading, thickness, resistance and resistivity measurement device
Surface load	FLEX ELECTRODE CHARACTERIZATION - Fully integrated automatic system for coating characterization: surface loading, thickness, resistance and resistivity measurement device
Resistivity	FLEX ELECTRODE CHARACTERIZATION - Fully integrated automatic system for coating characterization: surface loading, thickness, resistance and resistivity measurement device
Calendering	FLEX CALENDERING - Automatic system for high precision calendering of electrodes
Punch electrode	FLEX PUNCHING Fully automated system for electrode punching.
Assemble coin cell	FLEX COIN CELL ASSEMBLY Fully automated system for coin cell assembly
Store cell	FLEX COIN CELL ASSEMBLY Fully automated system for coin cell assembly
Close and store vessel	FLEX VESSEL STORAGE Automatic storage and handling system for formulation vessels
Export data	DASHBOARD Setup for data and workflow management, including real-time visualization

Powerful advantages

- Increase throughput
- Enhance reproducibility and quality
- Reduce raw material consumption and waste
- Enable digitalization
- Release brain power for other tasks
- Boost innovation

ARKSUITE

Workflow management software for automated systems.

ARKSUITE is an integrating software platform that serves as a central control centre for orchestrating multiple instances (incl. 3rd-party devices) – global experiment design, experiment execution, scheduling, inventory management, data management, digital twin.

Application Showcase

Integrating additional services such as LIMS, web services, and other auxiliary tools further enhance the overall process. The inclusion of 3rd -party devices e.g. for analysis / testing completes the workflow provides full end-to-end control and comprehensive data capture.

- **Flexibility:** Highly flexible design supports essentially any interface using IoT and Internet 4.0 concepts.
- **Data capture:** Comprehensive experimental data capture, including universal execution time stamps.
- **Collaboration:** Central database services support ease of linking multiple systems, labs and even sites for uninhibited data share and collaboration (physical and / or cloud-based server solutions).
- **Exceptional control:** Radical Digital Twin provides real-time top-level viewing and control of integrated systems and/or labs.



Conclusion

By automating key processes like slurry formation, electrode production to cell assembly and characterization, Chemspeed's FLEXSHUTTLE significantly increases throughput, reproducibility, quality and reduces material waste. The integrated workflow management ARKSUITE software allows seamless control and data capture enabling researchers to focus on innovation rather than manual tasks. This comprehensive solution paves the way for accelerated battery development.



AUTO-DESICCATOR CABINETS

Humidity-sensitive samples are safely stored in our reliable auto-desiccator cabinet



Features:

- › Auto-electronic dry unit
- › Height-adjustable shelves
- › Temperature and humidity display
- › Space saving double-stacked cabinets
- › Clear observation of samples
- › Easy installation and relocation
- › Built in door lock device for safe sample storage
- › Constant low interior humidity in the range of 20% and 60%

Relative Humidity	Application
45 to 60% RH	Painting, Stamps, Photographs, Antiques, Documents, etc.
40 to 45% RH	Camera, Lens, Microscopes, Films, Telescopes, Computer commodities, Audiotapes, Videotapes, Sliders, CDs, DVDs, etc.
30 to 40% RH	Semiconductor, Electronic components, IC components, PCB, Precision instruments, Electrical materials, Chemical materials, Industrial materials, etc
Below 30% RH	Semiconductor components, Ceramic powders, Seeds, Spices, Reagents, Laboratory samples, etc.



Battery components Analyses using AFM-in-SEM LiteScope™

An Overview of NenoVision's Litescope Battery Materials Solutions

Performance and longevity of batteries is intrinsically linked to the materials used in their construction. This application note presents an overview of key material components within cell and battery technologies, such as cathodes, anodes, and electrolytes, in both solid and liquid states.

Enhanced by NenoVision's LiteScope, this article is intended to provide a foundational understanding of the raw active materials involved in battery technology, emphasising their roles in energy storage and transfer mechanisms.

Keywords or phrases: Battery, cathode, anode, electrolyte, AFM-in-SEM, NenoVision
LiteScopeSWILE

Introduction

Energy storage devices are crucial to today's technology. Understanding their features, performance, aging, and capacity is vital.

Most high-end batteries are Li-ion, with active materials extremely susceptible to atmospheric contamination and degradation.

NenoVision's battery materials solution with LiteScope provides a complete hardware and measurement workflow approach. It allows for an air-free sample transfer system that prevents contamination by oxygen and humidity, while ensuring uncompromised sample surface preparation.

The imaging power of AFM-in-SEM provides a complex and site-specific understanding of the electrical and chemical properties of battery components.

Application Showcase

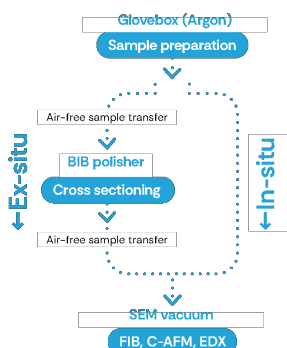
Measurement Workflow

1. Ex-situ sample preparation using Sample Transfer System

This option allows larger cross-section preparation in specialized instruments while maintaining the sample surface in the necessary environment, even during transfer and AFM-in-SEM measurement.

2. In-situ sample preparation using Focused Ion Beam

LiteScope enables safe AFM probe positioning for large stage tilts, preserving the tip from redeposition and allowing the use of FIB to cut a trench anywhere on the sample. This allows measurement of the uncovered surface using AFM-in- SEM technology.



Cathode Tape Inspection

Solid State Batteries (SSBs) show promise over Li-ion batteries with **higher energy density, longer lifespan, and improved safety**. A cathode tape composed of Lithium Nickel Manganese Cobalt Oxide (NMC) particles was opened after 200 cycles in a glovebox, cross-sectioned ex-situ, and measured using AFM-in-SEM (Measurement Workflow 1).

SEM imaging identified the polished area of interest. The EDS map showed the cathode tape's composition, including the solid electrolyte, NMC particles, and carbon additive. C-AFM confirmed the carbon additive's conductivity and its role in connectivity.

material functions or failures without altering the sample surface.

Key benefits and features

Fast and easy sample transfer: Small evacuation time is needed to exchange the samples.

No air or humidity exposure: Air-sensitive samples are protected from surface contamination or oxidation in a vacuum or inert gas atmosphere at all times.

Complete measurement workflow: A comprehensive procedure for the cross-sectional analysis of complex battery components and materials testing.

Upgradation to SEM solution: Extended possibilities are enabled using FIB/GIS prep, AFM, C-AFM, KPFM, phase imaging, SE, BSE, EDX, Fz spectroscopy.

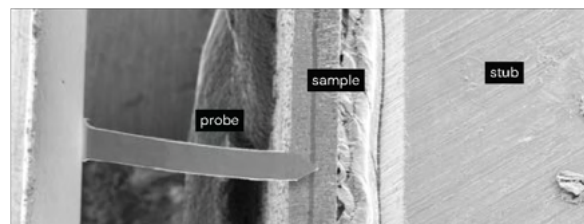
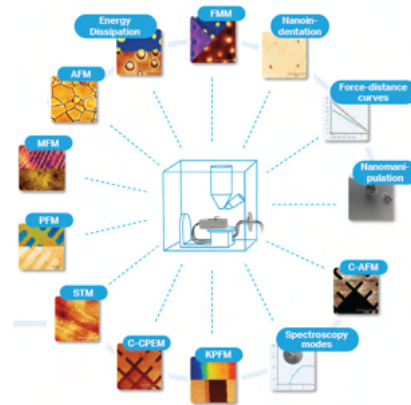
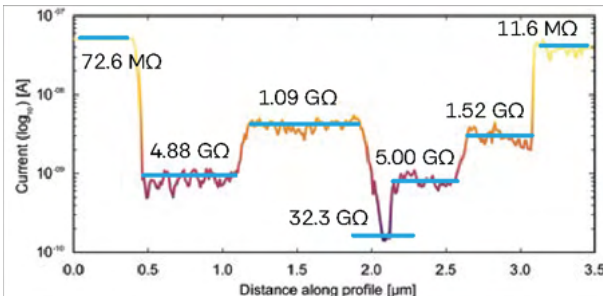


Figure 1: SEM overview: probe navigation to cross-sections



Application Showcase

/ Current profile with calculated resistivity



/ SEM

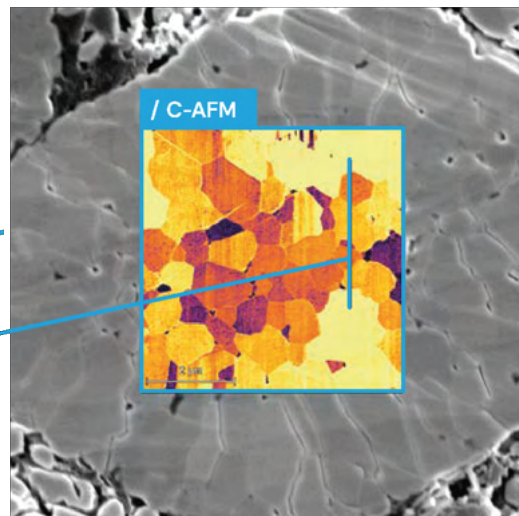


Figure 2: Complex conductivity distribution inside the secondary NMC particle is revealed by C-AFM

IntraParticle Conductivity

The cycling of batteries involves the transport of lithium ions from the cathode to the anode and vice versa, which causes the electrode particles to expand and contract. Over many cycles, the battery performance decreases. Understanding these degradation mechanisms is crucial for longer battery lifetime and better performance.

The C-AFM was employed to image a secondary particle from an NMC cathode of a liquid electrolyte (LE) battery after 200 charge-discharge cycles.

It revealed an interesting conductivity structure of primary particles, and the cracks formed between them during cycling. While there is an overarching tendency for the primary particles to be less conductive closer to the particle centre, another effect causes seemingly random conductivity variations.

Local C-AFM proves, that some of the primary particles lost electrical contact with their neighbours, probably due to cracks, and became disconnected. The effect is not negligible, as the current profile taken across a few grains shows differences in orders of magnitude, which then influences (decreases) overall battery performance.

Conclusion

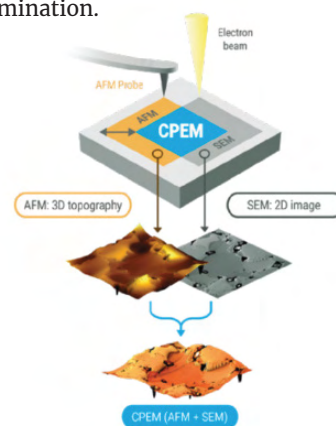
LiteScope™ solution for battery components analyses

Complete Workflow

Delivers a complete workflow for sample surface preparation, air-free sample transfer, site-specific electrical and chemical properties measurements, and data post-processing.

Battery components and materials testing

This setup enables the characterization of performance and failures, understanding of cycling effects, active material degradation, inter/ intraparticle connectivity, and delamination.



Application Showcase

Sample Transfer Module

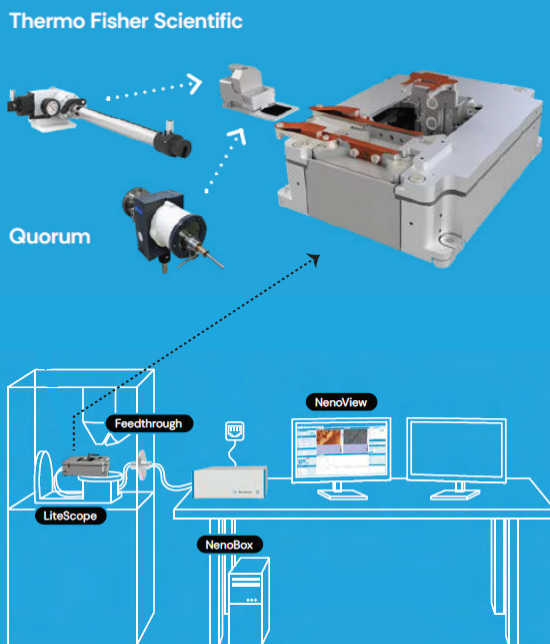
Dedicated Module for AFM-in-SEM LiteScope provides an effective solution for safe sample transfer under a controlled environment.

The module of compact design is compatible with most already existing sample transfer systems and their accessories.

LiteScope Setup

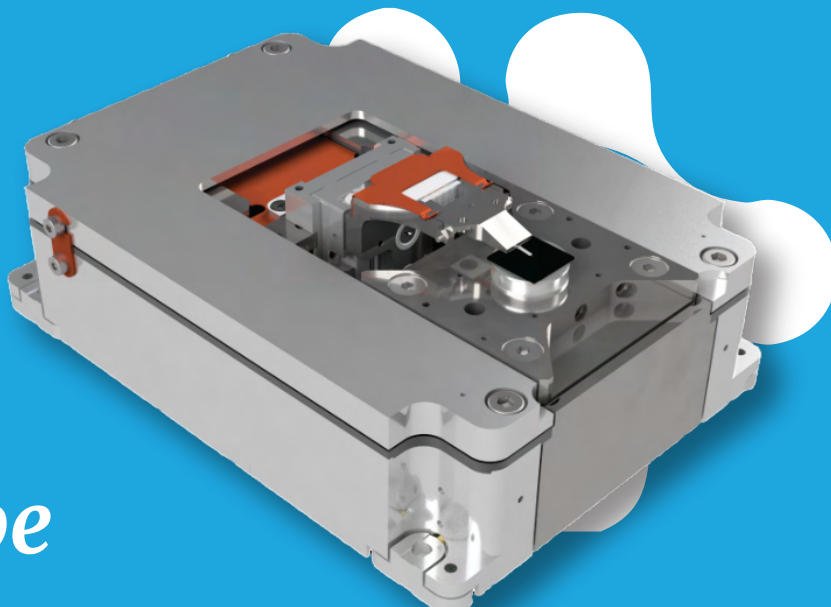
NenoVision combines tradition and expertise with unique solutions in nanoscale AFM-in-SEM microscopy.

Thanks to its optimized design, the AFM LiteScope seamlessly integrates into most SEM systems produced by Thermo Fisher Scientific, TESCAN, ZEISS, Hitachi, Jeol, and their accessories.



Application areas

- › Cell and battery components
- › Raw active materials
- › Cathodes
- › Anodes
- › Solid electrolytes
- › Liquid electrolytes



LiteScope AFM-in-SEM



Introducing the Next Generation Battery Tester The Series 6000

Advanced Multiple Level Pulse – "AMLP"
Enables creation of the most complex pulse profiles available



Desktop Tester



Battery Test System

- ⚡ AMLP steps can consist of a set of up to 15,000 levels.
- ⚡ Each level can be constant current, power, or resistance.[†]
- ⚡ Each level will be a minimum of 100 microseconds and a maximum of 15 seconds.
- ⚡ Levels can be programmed in 100-microsecond increments.
- ⚡ All levels in a particular AMLP step must be in charge, or all must be in discharge.
- ⚡ Voltage end condition checked every 100 microseconds.
- ⚡ When the voltage end condition is met, the test will branch to a user-selected step elsewhere in the test procedure.
- ⚡ Record data as fast as every 100 microseconds.

Evaluating AFM as an analysis tool for graphene

Nanosurf's AFM Solutions for Graphene Research

Attomeric Force Microscopy is a powerful tool for characterizing 2D materials, particularly graphene. This application reviews the key advantages of AFM for characterizing and manipulating these nanomaterials.

Example measurements of flake thickness, detailed analysis of graphene growth quality and visualization of moire patterns arising from lattice mismatch in stacked 2D layers, using the AFM are discussed here.

Keywords: Atomic Force Microscopy, AFM, graphene, characterization, Nanosurf

Introduction

What is graphene?

Graphene is the most famous member of the 2D materials family: a sheet of covalently bonded carbon atoms in a hexagonal lattice in which the thickness has been reduced to a single atom. This unique nanomaterial is extraordinarily strong and has the highest known thermal and electrical conductivity. It was awarded the Nobel prize for Physics in 2010, for research done by Andre Geim and Konstantin Novoselov.

There are many other 2D materials that are being actively explored. A collective group of graphene-like structures is known as xenes – which are also monolayers of a single element. For example, single layer of black phosphorus, phosphorene, is a promising material for transistors. Other examples are silicene (silicon), germanene (germanium), and stanine (tin), all exhibiting a hexagonal structure like graphene with

Application Showcase

various degrees of buckling.

Hexagonal boron nitride (h-BN) has the same overall structure as graphene but replaces the carbon atoms with alternating boron and nitrogen atoms. Finally, members of another popular class of 2D materials are transition metal dichalcogenides with the chemical formula MX_2 , where M is a transition metal such as tungsten or molybdenum and X is a chalcogen such as Sulphur, selenium, or tellurium.

Interest in stacking of graphene on itself or other 2D materials is currently gaining traction. An angular or lattice mismatch has been shown to create different electrical properties of the layered stack. This opens the door to creating new devices in a bottom-up approach, stacking multiple layers of 2D materials under such angles that allow tuning of the properties.

However, as relaxation processes after deposition occur, control measurements are needed to verify the angular mismatch between the layers.

Why AFM?

AFM has become the instrument of choice for studying nanomaterials for two key reasons: resolution, and availability of many different modes enabling zcomprehensive characterization of a nanomaterial, including its mechanical and electrical properties beyond the topography. The exceptional x-, y-, and z resolution are important due to phenomena close to the atomic scale. The resolution of a commercial AFM ranges from less than a few nanometres all the way to atomic resolution laterally, and better than 0.1 nm vertically. This makes AFM one of the few types of instruments that can attain the resolution required to measure nanosheets that are only a few angstroms thick.

Another advantage of AFM that has real-life implications is the available suite of measurement modes to assess electrical and mechanical properties simultaneously to the topography. These modes can be used to study those additional properties in detail, or

simply as a contrast mechanism to evaluate the quality of grown graphene or the angular mismatch between stacked layers of graphene. This makes AFM an indispensable tool for device design that relies on the stacking of 2D materials. Finally, the AFM tip can be used to manipulate samples at the nanoscale. In the case of graphene, it can, for example, be used to cut through graphene sheets. The two halves of a single graphene sheet cut in two have the same crystal orientation, enhancing the control of the angular mismatch during stacking.

Besides these imaging properties, an additional motivation for utilizing AFM originates from its small footprint, allowing it to be placed inside a glovebox. This is a prerequisite to studying graphene in combination with 2D materials that are sensitive to the presence of oxygen or humidity.

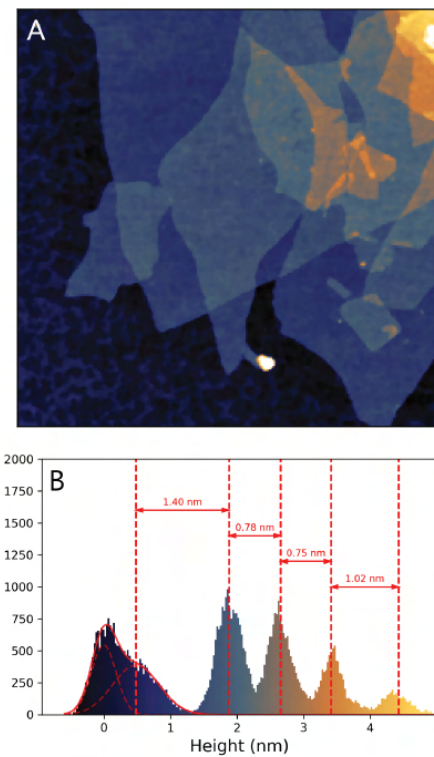


Figure 1. Measuring the thickness of multilayer graphene. (A) AFM topographical image of graphene oxide with lateral dimensions of 5.11 x 5.11 μm^2 . (B) Histogram of the heights in (A) showing the thickness of the first 4 layers.

Sample courtesy: Nanotech Energy, USA.

Application Showcase

Applications

1. Flake thickness: The first example illustrates the superb resolution of AFM. Figure 1 reveals several stacked layers of graphene oxide, enabling analysis of the thicknesses of the individual layers. A corresponding height histogram of the measurement shows the thinnest layer to be a mere 0.75 nm. This image demonstrates the exceptional vertical resolution of AFM at the level required to study 2D materials.

2. Graphene growth analysis: An example of the ability to check the quality of graphene is shown in Figure 2. The sample consists of graphene grown by chemical vapor deposition (CVD) on copper.

The copper substrate is not atomically flat, sometimes obscuring the edges and fine features of the flakes. The copper was oxidized after the deposition, resulting in the height of the oxidized copper exceeding that of the graphene flake in the topography (Figure 2A and 2C).

The lateral force image (Figure 2B) shows a lower friction on the graphene (blue contrast) compared to the copper substrate (green contrast) that assists analysis of the graphene coverage of the copper substrate, since edges have a sharper contrast in the friction channel than in the topography. In addition, the friction image clearly shows a higher friction in the centre of the flake, identifying the growth seed point of the flake that is not visible in the topography.

Kelvin probe force microscopy (KPFM) was also used to analyse this sample (Figure 2D). Conventionally, KPFM is used to analyse the contact potential difference (CPD) between tip and sample, and under vacuum conditions even the work function. As expected, graphene and the oxidized copper show a different CPD, graphene having a lower value. More importantly, the CPD image shows a heterogeneity on the graphene, with some fine lines and areas on the graphene flakes that are not recognizable in the topography, thus enhancing the quality assessment of the graphene deposition process by AFM.

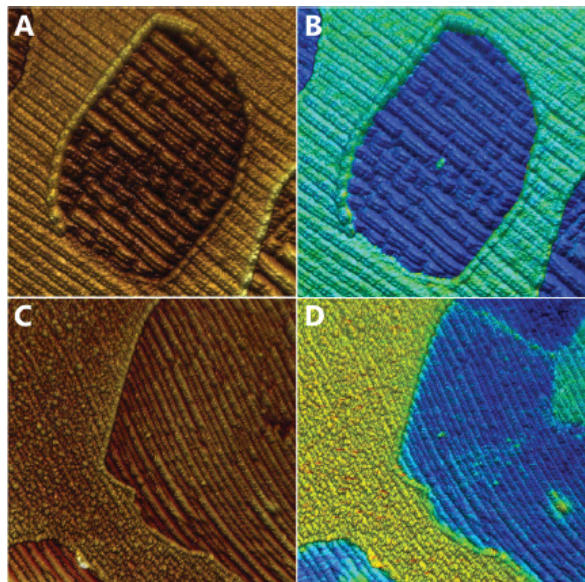


Figure 2. Quality control of chemical vapor deposition (CVD) grown graphene on post-oxidized copper by lateral force imaging and KPFM. (A) Topography and (B) friction force images, simultaneously recorded. The friction was calculated from the difference between the forward and backward lateral deflection channels. Scan size: 5 x 5 μm^2 . (C) Topography and (D) contact potential difference images. Scan size 10 x 10 μm^2 .

Sample courtesy: Nanotech Energy, USA.

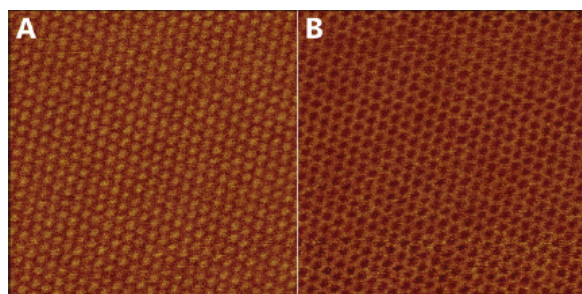


Figure 3. Moiré super lattice of twisted graphene on hBN imaged in PFM mode at the contact resonance frequency. (A) amplitude and (B) phase. Scan size: 154 x 154 nm 2 .

Sample courtesy: Nanoelectronics group TIFR, India.

3. Lattice mismatch: The interaction between the AFM tip and a graphene layer also depends on the interaction of the graphene layer with the layer underneath.

In the presence of an angular mismatch, the interaction varies periodically with a lattice constant depending on

Application Showcase

the angular mismatch. This regular pattern, also called moiré super lattice, can be visualized using AFM, for example by piezo-response force microscopy (PFM)¹ or force modulation², oscillating the cantilever at the contact resonance frequency. A cantilever with the tip in contact with the sample has different resonances than a free-swinging cantilever.

The first contact resonance is very sensitive to the mechanical properties of the sample. The contact resonance can be measured directly with a phase-locked loop or dual frequency resonance tracking, or indirectly but more straightforwardly by detecting the phase and amplitude of the cantilever excited at a fixed frequency on the contact resonance peak. This contact resonance frequency can be determined from a thermal tune spectrum recorded with the tip in contact with the sample.

The angular mismatch between two layers of graphene can be calculated from the periodicity of the moiré superlattice.

Figure 3 shows the phase and amplitude response obtained by imaging a double layer of twisted graphene, clearly displaying the moiré pattern caused by an angular mismatch. The cantilever was electro-statically excited in PFM mode at the contact resonance frequency. Based on the lattice constant of the moiré pattern, the angular mismatch of this sample amounted to 2.2°.

Figure 4 shows the phase response measured in force modulation imaging mode on a DriveAFM². Here, the cantilever was photothermally excited on the contact resonance peak. The 192 nm wide image of Figure 4A shows a lattice with some distortion, indicating a variation in the angular mismatch, but still giving multiple diffraction spots in frequency space after Fourier transformation (Figure 4B).

The frequency of $1/(7.26 \text{ nm})$ of the (2;2) diffraction spot close to the fast scan axis converts to a lattice constant of 29 nm in real space.

This is 117 times larger than the lattice constant of graphene, portraying an angular mismatch close to 0.5°. Recording a 68 nm wide image (C) with 1024 x 1024 px² does not only show the moiré super lattice, but also the atomic lattice. A digital zoom of 17 nm in width of the phase signal is shown in Figure 4D, to enhance the visibility of the lattice in real space and Figure 4F shows the Fourier transform of the phase signal. The atomic lattice was used to verify the lattice of the moiré super lattice.

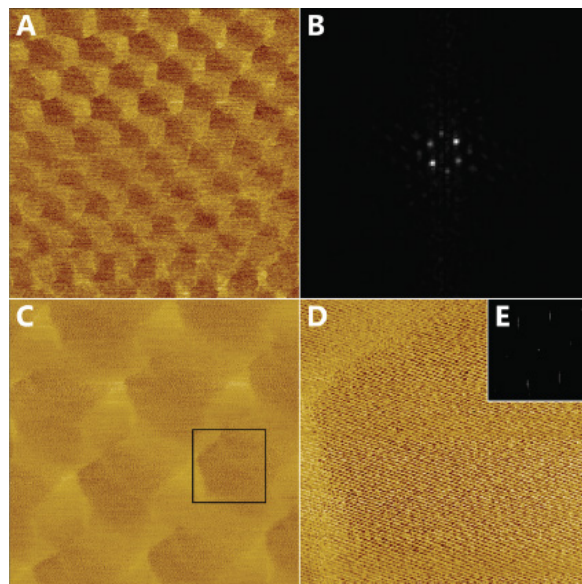


Figure 4: Moiré super lattice of twisted graphene on hBN imaged in force modulation mode on the contact resonance frequency. (A) phase image with scan size of 190 x 190 nm² (B) Center part of the Fourier transform image used to determine the lattice constant of the moiré pattern (C) phase image of 68 x 68 nm² area rescanned with 1024 x 1024 px² containing both the moiré superlattice and atomic lattice. (D) Digital zoom of the (C). (E) Fourier transform showing the diffraction spots from the atomic lattice.

Sample courtesy: Nanoelectronics group TIFR, India.

4. Cutting graphene: As mentioned, not only can the AFM tip be used to measure, but also to manipulate materials on the nanometre scale. Figure 5 shows an example of a multi-layer stack of graphene that was cut with an AFM tip in nanolithography mode. The experiment was carried out on a FlexAFM. In lithography, cutting can be controlled by several parameters, such as force, speed, and direction. At the same time a DC or AC voltage or combination of both can be applied between tip and sample to influence the depth of the cut.

Application Showcase

It is believed that the cutting mechanism occurs via local anodic oxidation of the surface³⁻⁵. The high voltages near the tip dissociate H₂O into H and OH groups, which oxidize the graphene. The tip induced mechanical stress then fractures the graphene at the locations it was oxidized. This is the reason why the relative humidity surrounding the tip plays an important role in graphene cutting. The environmental control add-on allows fine control of the humidity around samples.

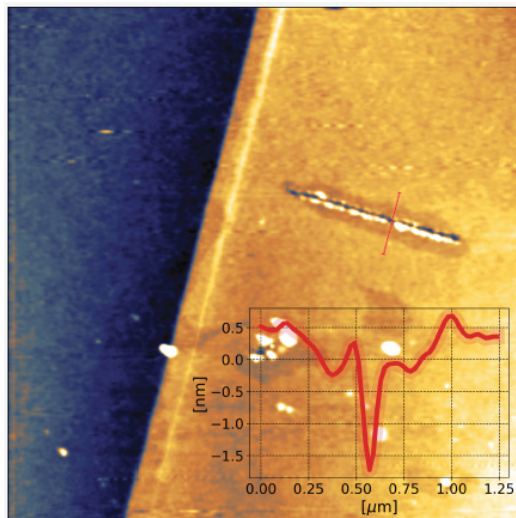


Figure 5. Cutting graphene by AFM lithography. AFM topography image of a multilayer graphene flake on Si substrate with lateral dimensions of 10 x 10 μm^2 . Cuts were obtained by applying a 10V AC voltage at 500 kHz to the tip of a BudgetSensors ElectriTip190E cantilever ($k = 48 \text{ N/m}$ nominal) and following the designated path in Static Force Mode with an applied force of 5 μN at a speed of 100 nm/s. The relative humidity was 42%.

Sample courtesy: Kim group, Harvard University, USA.

Conclusion

Graphene and other 2D materials like xenes – or transition metal dichalcogenides – are a fast-growing topic of interest among leading nanomaterials researchers, with exciting applications in transistors, sensors, and optoelectronics. AFM is uniquely suited to study such materials thanks to its impressive resolution well below a nanometre, capable of clearly showing the atomic lattice and atomic steps. As a multifunctional characterization tool, AFM can measure and correlate multiple important properties of these materials to

to better understand and characterize them. The detection of moiré patterns is one example of this type of characterization. In addition, AFM can be used to locally manipulate 2D materials.

In summary, this makes AFM indispensable for the study of graphene and other 2D materials in search of ultimate integration into devices and other applications.

References

1. McGilly et al 2020 *Nat. Nanotechnol.* 15, 580– 584
2. Adams et al 2021 *Rev. Sci. Instr.* 92, 129503
3. Puddy et al 2011, *Appl. Phys. Lett.* 98, 133120
4. Masubuchi et al 2011, *Nano Lett.* 11, 4542–4546
5. Li et al 2018, *Nano Lett.* 18, 8011-8015

 nanosurf



DriveAFM

ULTRASONIC BATH

DUAL 40/80 KHz
HIGH FREQUENCY POWERFUL
CLEANING

HEATING UP TO 100 °C

AVAILABLE IN CAPACITIES
FROM 2.5 L TO 22 L

Ideal For Medical And Surgical
Instruments, Carburetors,
Industrial Machine Parts,
and Electronic Equipment.



Precision Cleaning For Sensitive Labware And Equipment



Scanning Microwave Microscopy (SMM) A Modern Alternative to Scanning Capacitance Microscopy (SCM)

Over the last few decades, the drive to miniaturize electronics has increased the demand for nano-electrical characterization methods. Understanding the local electronic material properties, such as conductance, dielectric constant, local capacitance and dopant density is critical for research and development of the semiconductor and microelectronics industries.

Atomic force microscopy (AFM) has been a key technology used to correlate topographical structures with local electronic properties at the nanoscale. Techniques such as conductive atomic force microscopy (CAFM) and Kelvin probe force microscopy (KPFM) allow for the measurements of local currents and electric surface potentials while scanning capacitance microscopy (SCM) maps the capacitance or local carrier density.

Scanning microwave microscopy (SMM) is unique in revealing buried structures that are prevalent in multilayered modern integrated circuits (ICs). These measurements are essential for applications in failure analysis, simulation of device performance, and optimization of semiconductor manufacturing processes.

Scanning microwave microscopy

SMM is a scanning probe technique that measures the interactions of a microwave between a sharp tip and the sample. The ratio between the power sent to the tip and the power received after being reflected at the tip-sample contact is expressed in the microwave reflection coefficient (S_{11} parameter). The S_{11} parameter is used to infer the tip-sample microwave impedance. The microwave impedance yields information about the local capacitance that can be used to determine the dielectric constant and the dopant density.

One of the main shortcomings of SCM, a technique similar to SMM, is that dopant density measurements are largely qualitative and cannot be applied to materials other than semiconductors. In contrast, SMM can be used to measure a range of materials including dielectric materials and metals¹, since it does not solely rely on the modulation of the depletion capacitance in the sample. Additionally, SMM operates at higher frequencies, leading to better sensitivity and the high precision electronics allow for calibrated and absolute measurements. While extraction of numerical data is possible analytically in SMM, in practice, calibration samples keep the experiment from quickly becoming complex. A typical SMM setup consists of a radio frequency (RF) wave source and a receiver working at a few GHz (Figure 1). In a pure S_{11} measurement, the transmitter and receiver both work on the same frequency, and only one main tone (or frequency) is observed in the frequency spectrum. The signal is transferred to and from the cantilever via a low loss coaxial cable. Because the typical port impedance is 50Ω and the tip-sample contact impedance is much higher, and matching circuit is usually required.

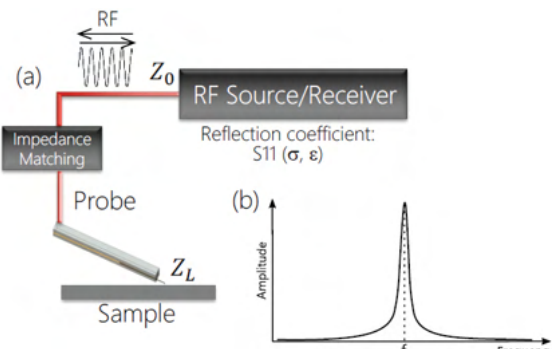


Figure 1. A schematic of a typical SMM setup: RF source/receiver electronics send the RF wave with impedance Z_0 through the transmission line to the probe (red). The sample-probe impedance is Z_L . The impedance matching circuit works as an “antireflection” medium between the low impedance Z_0 and high impedance Z_L . There is only one frequency peak (f_{RF}) in the spectrum and the amplitude and/or phase are tracked during scanning of the surface.

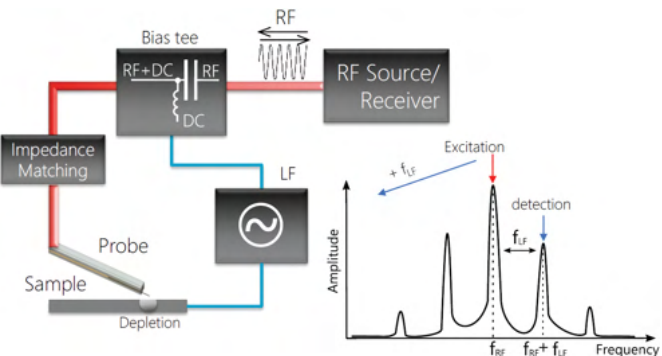


Figure 2. Schematic of a $dS11/dV$ measurement: a low frequency bias voltage (LF) is applied between the probe and the sample. The non-linear behavior of the tip-sample contact causes frequency mixing between the RF and the LF signals. The frequency spectrum exhibits sideband peaks on both sides of the main RF tone (plot). The frequency of the mixed product, i.e. $f_{RF}+f_{LF}$, is used for detection of $dS11/dV$

Once the RF electromagnetic wave leaves the coaxial cable, it starts radiating into free space. This can cause topographic crosstalk in the $S11$ measurement. In semiconductor materials, an AC voltage bias can modulate the dopant density in the sample under the tip, and therefore the $S11$ signal. Tracking the change of $S11$ relative to the change of the bias voltage (similar to lock-in amplification) minimizes topographic crosstalk. This is called the $dS11/dV$ measurement, which yields information that is similar to the conventional dC/dV measurement in SCM.

$dS11/dV$ only works on semiconductors. To realize this measurement, a low frequency (LF) modulation is applied between tip and sample. The non-linearity in the tip-sample interaction causes frequency mixing between the RF and LF waves. Hence, it gives rise to sideband peaks on both sides of the main tone (Fig. 2). The detection of the sideband signal is performed by mixing the signal back down to the LF frequency and demodulating it using a lock-in, or by directly measuring amplitude and phase of the sidebands. The latter is preferred as it eliminates $1/f$ noise.

Scanning microwave microscopy

Applications of SMM include measuring dopant densities and failure analysis in semiconductor devices. We demonstrate an example of each:

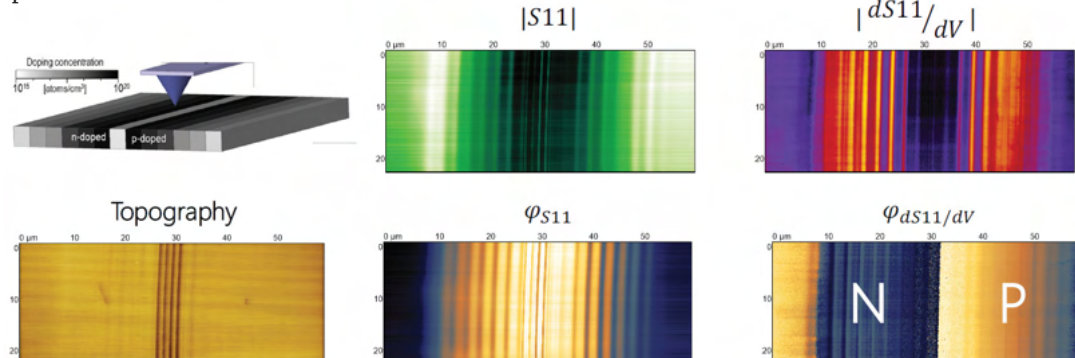


Figure 3. An $S11$ measurement (amplitude and phase) and a $dS11/dV$ measurement (amplitude and phase) of an Infineon SCM calibration sample. Clear contrast between the regions of different dopant density can be observed in both the $S11$ and the $dS11/dV$ measurements. The $dS11/dV$ measurement indicates polarity and the type of the dopant – n or p – can be determined. The schematic image of the sample is taken from Ref. 2.

Figure 3 shows the S11 measurement of the Infineon SCM calibration sample and good contrast can be observed on dopant densities in the range of 1015–1020 1/cm³. The dS11/dV measurement provides complementary data and the type of the dopant (n or p) can be observed in the phase image. The raw data in the SMM measurement is uncalibrated, and the calibration procedure has to be applied to the measured data to extract quantitative values for the capacitance, resistance, and the material parameters. Detailed description of calibration procedures for SMM can be found in literature^{2,3}.

Another sample that exhibits structures with clear differences in dopant type and concentration is a semiconductor SRAM chip.

Figure 4 shows an SMM measurement of a device where device faults or relative changes in dopant concentration could be identified to evaluate device performance or potential sites for failure.

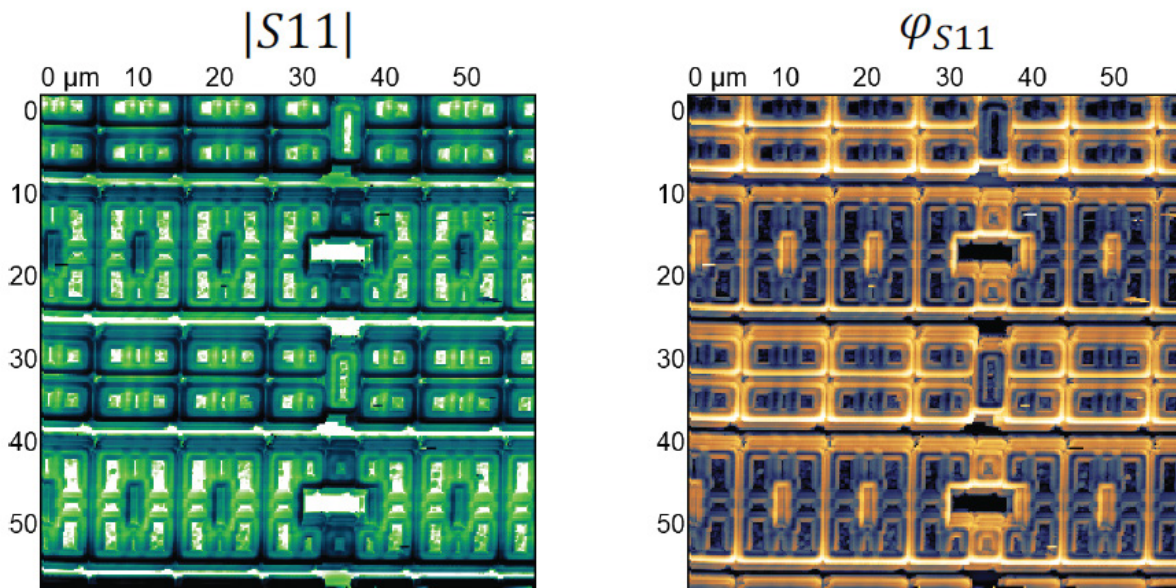


Figure 4. An S11 measurement (amplitude and phase) of a SCM sample, demonstrating high contrast between the areas of different doping levels.

Conclusion

SMM is a modern alternative to SCM that does not rely on the use of resonant circuits, to measure the S11 parameter or the microwave reflection coefficient. SMM is applicable to materials beyond semiconductors including dielectrics and metals. Calibration isn't required for many key applications such as for instance fault detection in the semiconductor industry. Still, when using relatively simple calibration procedures, analytical calculations become possible, and material properties can be determined quantitatively.

References

1. J. Hoffmann et al., Appl. Phys. Lett. 105 (2014) 013102
2. Brinciotti et al., Nanoscale 7 (2015) 14715
3. Hoffmann J., et al., IEEE-NANO (2012)

Guide:

Optimized Annealing of TiO_2 and Tin for Enhanced Crystallinity and Reduced Thermal Stress



Annealing is a critical heat treatment process in materials science, particularly for modifying the physical and chemical properties of various materials. Both titanium dioxide, widely used in optical, photocatalytic and nanomaterials research and titanium, a key component in solder, electronics, glass, alloys and coatings, are materials that are greatly exploited.

Effect of annealing on TiO_2

Titanium dioxide (TiO_2) has three main crystal structures: anatase, rutile, and brookite. Annealing has a profound effect on the crystallinity of TiO_2 , influencing phase transitions, crystallinity and grain size. Generally, with increasing annealing temperature, anatase transforms into rutile, a thermodynamically stable form in higher temperatures. The temperature causing these transformations depends on the TiO_2 material, annealing conditions and nature of impurities.

Annealing also improves crystallinity within TiO_2 , causing the amorphous form to change into a more crystalline structure, resulting in improved optical and electrical properties.

Effect of annealing on Sn

Tin has several crucial roles in various applications- as solder for electronic connections, protective coating for prevention of metal corrosion and as float glass in glass manufacturing.

Tin has the tendency to accumulate internal stress during manufacturing processes like rolling, casting etc. Annealing relieves this internal stress by providing thermal energy required to rearrange its structure, thus preventing cracking or even permanent failure. Annealing also influences metal properties contributing to grain growth and recrystallization.



This guide outlines the procedure for annealing TiO_2 or tin at approximately $500^{\circ}C$ with slow ramping.

Procedure

› Sample Preparation:

Prepare the TiO_2 or tin samples to be annealed. Ensure they are clean and free from contaminants.

› Loading the Furnace:

Place the samples in the Muffle Furnace chamber. Ensure they are positioned to allow uniform heating.

› Setting the Parameters:

- Temperature:

Set the furnace to ramp up to $500^{\circ}C$ gradually. Slow ramping is essential to prevent thermal shock and ensure uniform heating.

- Ramp Rate:

Program the furnace to increase the temperature at a controlled rate (e.g., $5^{\circ}C$ per minute) until it reaches the target temperature.

- Hold Time:

Once the temperature reaches $500^{\circ}C$, maintain this temperature for the desired hold time (e.g., 2 hours) to allow thorough annealing.

› Cooling:

After the hold time, allow the furnace to cool down gradually to room temperature. Slow cooling helps in minimizing thermal stresses.

› Unloading the Samples:

Carefully remove the annealed samples from the furnace once they have cooled down.

Key Advantages of Muffle Furnace Annealing:

➤ **Controlled Heating Environment:**

Muffle furnaces provide a contained environment ensuring that the material is heated to the desired temperature and held there for the required duration.

➤ **Uniform Temperature Distribution:**

Even heat distribution throughout the chamber, essential for achieving consistent material properties.

➤ **Protection from Contamination:**

The "muffle" itself refers to the chamber that isolates the material from direct contact with the heating elements and combustion byproducts. This is vital for preventing contamination, especially when annealing sensitive materials.

➤ **Versatility:**

Muffle furnaces can be used for a wide range of annealing applications, including:

- Relieving internal stresses in metals.
- Softening metals for further processing.
- Modifying the microstructure of materials.
- Heat treating various materials.

➤ **Precise Temperature Control:**

Modern muffle furnaces are equipped with digital controllers, which allow for very accurate temperature settings and monitoring. This precision is essential for achieving the desired annealing results.

➤ **Safety Features:**

Built-in safety mechanisms protect both the user and the equipment during high-temperature operations.

Conclusion

Annealing significantly improves material properties of TiO_2 and tin. It brings changes in phase transitions, enhances crystallinity and controls grain size. Alterations in these properties make them more suitable for their applications in optical, electric, photocatalytic, nanomaterials research.

Similarly, annealing of tin relieves internal stress and promotes recrystallization, thereby increasing its performance for use in solder, coatings and alloy formation.

Such precise control is offered by muffle furnace annealing, allowing manipulation of microstructure for desired outcomes.

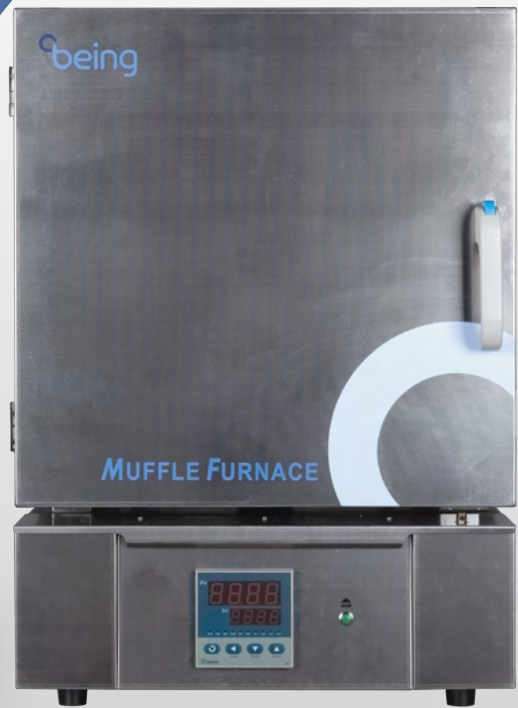
Features:

- The structural design and safety meet international electrical safety standards
- High quality heating elements, corrosion-resistant ceramic fiber furnace
- Housing made of sheets of cold-rolled steel, finished by powder coating

Efficient and Reliable High-Temperature Heat Treatment Solutions

Maximum
Temperature up to **1200 °C**

Available in 7 L and 12 L



MUFFLE FURNACE

cbeing Laboratory
Instrument
Manufacturer

Suitable for quenching, annealing, tempering small steel parts, pre-treatment for sintering, ashing analysis, etc. of metal, stone tools and ceramics in **material science and characterization laboratories**.

Product Highlight



Labstation i
INERT GAS GLOVEBOX WORKSTATION

Inert Gas *Glovebox* Workstation

Synthesis and characterization of novel and delicate materials require a setting of absolute purity and precision. Such manipulations and reactions are carried out in sealed environments isolating the contents within from the external atmosphere. Inkarp Instruments' Labstation i inert gas glovebox workstation is specifically designed to meet these challenges.

Labstation i's inert gas management systems maintain the lowest oxygen and moisture levels of less than 1 ppm, creating ideal conditions for working with the most air- and moisture-sensitive materials.

The modular design of the glovebox allows for expansion from 2 port to 4 port, allowing researchers flexibility to choose based on their needs.

*An Inkarp Product



Features

- Closed loop recirculation
- Attainable oxygen and moisture level < 1 ppm
- Modular design for extension in future
- Smart Energy Mode feature
- Automatic control of antechamber
- Automatic box purging function
- Negative and/or positive pressure operation
- Foot pedal switch for pressure adjustment
- Large purification column to absorb 44 L of oxygen and 1850 g of moisture.

Product Highlight

Applications

Gloveboxes are used in a variety of industries and in research where handling air- and moisture- sensitive materials and controlled environments is critical to attain the desired outcome.



Battery Research/Manufacturing:

Electrolyte handling, electrode preparation, battery assembly.



OLED/Display Manufacturing:

Handling of organic materials, deposition processes.



Semiconductor Industry:

Wafer handling, etching, and deposition processes.



Energy Research:

Battery development (lithium-ion, etc.), fuel cell research, and solar cell fabrication.



Automotive Industry:

Research and development of advanced materials for vehicles.



Nuclear Industry:

Handling of radioactive materials and waste.

Product Highlight

GLOVEBOX TECHNICAL DATA

Box Structure	Modular Design
Material	Stainless Steel (US304, 1.4301)
Leak Rate	< 0.01 vol%/h
Window	Safety glass (thickness 10 mm) or Polycarbonate (thickness 10 mm)
Glove Ports	Black anodised Al or POM Polymer, port diameter 220 mm
Gloves	Butyl rubber (thickness 0.4 mm)
Light	LED Lamp
Feedthroughs	4xDN40KF Flange
Dust Filter	Inlet/Outlet, HEPA H13
Electrical Feedthrough	1
Shelves	6 on rear panel with adjustable height

MAIN ANTECHAMBER TECHNICAL DATA

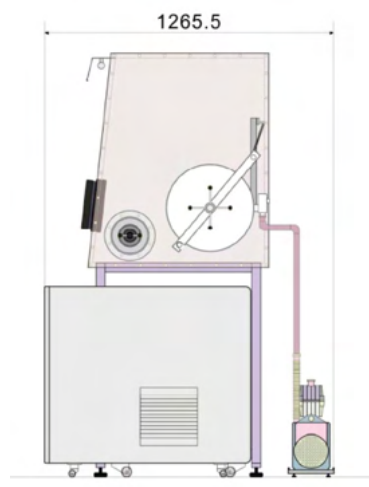
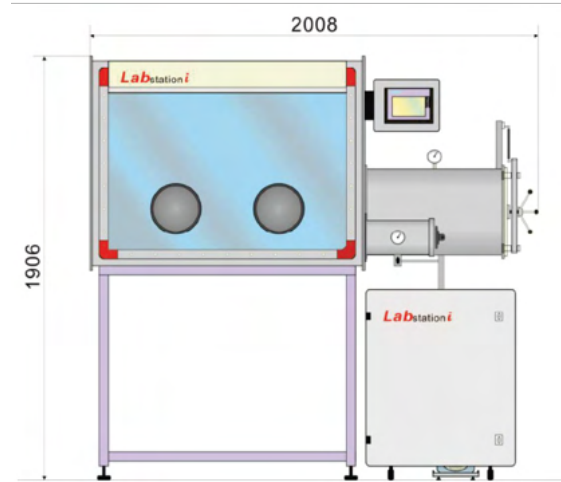
Type	Cylindrical
Material	Stainless Steel
Leak Rate	< 10 ⁻⁴ mbar l/s
Sliding Tray	Stainless Steel (US304, 1.4301)
Doors	Al, anodised (thickness 10 mm)
Door Lock	Door closing mechanism with spindle handle for one hand operation
Pressure Gauge	Analog Display
Vacuum/Refill Process	Automatic, PLC Control

MINI ANTECHAMBER TECHNICAL DATA

Type	Cylindrical
Material	Stainless Steel (US304, 1.4301)
Doors	Al, anodised (thickness 10 mm)
Vacuum/Refill Process	Manual valve

GAS PURIFICATION SYSTEM TECHNICAL DATA

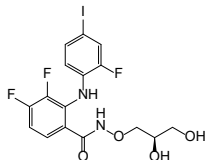
Attainable Purity Level	H ₂ O <1 ppm, O ₂ <1 ppm
Number of Purifier Columns	1 or 2
Regeneration	Automatic Program Controlled by PLC
Control Unit	SIEMENS PLC
Box Pressure Control	Automatic Pressure Control with foot switch (+/- 15 mbar)
Vacuum Pump	Option 1: RV12 flow rate 12 m ³ /h Option 2: DRV10Y flow rate 10 m ³ /h
Blower (50 Hz)	0-90 m ₃ /h with frequency controller
Regeneration Gas	N ₂ /H ₂ or Ar/H ₂ mix. (H ₂ 5-10 %)
Working Gas	N ₂ , Ar or Helium
Recirculation Control	Electro-pneumatic
Heat Exchanger	Included
Function	Automatic Box Purging Automatic Antechamber Control Smart Energy Mode



Watch here
to know more

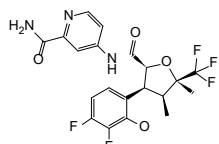


Recent novel FDA approved drugs



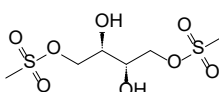
Mirdametinib

A kinase inhibitor, mirdametinib (Gomekli) treats neurofibromatosis type 1 in adults and paediatric patients who have symptomatic plexiform neurofibromas not cooperative to complete resection.



Suzetrigine

Suzetrigine (Journavx), a non-opioid, small molecule analgesic, that treats severe acute pain. It is a sodium channel blocker that targets a pain signalling pathway in the peripheral nervous system.



Treosulfan

Treosulfan (Grafapex) an alkylating drug is indicated in combination with fludarabine as a preparative routine for allogeneic hematopoietic stem cell transplantation in adult and pediatric patients >1 year old with Acute Myeloid Leukemia or Myelodysplastic Syndrome

Datopotamab deruxtecan (Datroway), an antibody drug conjugate made up of a monoclonal antibody and a topoisomerase inhibitor, used for the treatment of metastatic HR-positive, HER2-negative breast cancer and nonsquamous non-small cell lung cancer (NSCLC), in patients who have received prior systemic chemotherapy.

Industry Buzz

Vizag Pharma & Lab Expo

Visakhapatnam, 2025



MIT-Manipal:
International Conference on Advanced
Functional Materials and Applications (ICAFMA-2025)

A sneak-peak at our events

CATALYSTCue invites scientists and industry specialists to share their expertise through articles on emerging scientific breakthroughs and instrumentation.



Please write to us at **info@inkarp.co.in**

CATALYSTCue is now available in digital format.



Scan the QR Code to leave your valuable feedback

For latest news, insights, and discussions in the world of science, follow us on

Disclaimer: CATALYSTCue provides a platform for diverse perspectives. The views and opinions expressed in the articles and interviews are solely those of the authors.

Hei-VAP Industrial with glassware R

Speed range:

6 – 160 rpm

Heating bath volume:

18 L H₂O / 14 L oil

Temperature range of heating bath:

20 – 100 °C H₂O / 20 – 180 °C oil

Control:

Detachable, 7-inch touch panel, control knobs

- Clear visible monitoring
- Increased throughput at reduced energy consumption
- Intuitive touch screen



Your Knowledge... Our Solution...!

Authorised India Partner

Inkarp Instruments Pvt Ltd

Plot No - 5A/10-11, 3rd Floor, IDA Nacharam Road No. 1, Nacharam - Chilka Nagar Road, Hyderabad – 500076.

📞 040 27172293/5088 📩 info@inkarp.co.in

analytica Anacon India 23-24-25 April 2025, Mumbai
INDIALABEXPO Booth No: G031